



**University of
Zurich**^{UZH}

**Zurich Open Repository and
Archive**

University of Zurich
University Library
Strickhofstrasse 39
CH-8057 Zurich
www.zora.uzh.ch

Year: 2017

A survey of dual active galactic nuclei in simulations of galaxy mergers: frequency and properties

Capelo, Pedro R ; Dotti, Massimo ; Volonteri, Marta ; Mayer, Lucio ; Bellovary, Jillian M ; Shen, Sijing

Abstract: We investigate the simultaneous triggering of active galactic nuclei (AGN) in merging galaxies, using a large suite of high-resolution hydrodynamical simulations. We compute dual-AGN observability time-scales using bolometric, X-ray and Eddington-ratio thresholds, confirming that dual activity from supermassive black holes (BHs) is generally higher at late pericentric passages, before a merger remnant has formed, especially at high luminosities. For typical minor and major mergers, dual activity lasts 20–70 and 100–160 Myr, respectively. We also explore the effects of X-ray obscuration from gas, finding that the dual-AGN time decreases at most by a factor of 2, and of contamination from star formation. Using projected separations and velocity differences rather than three-dimensional quantities can decrease the dual-AGN time-scales by up to 4, and we apply filters that mimic current observational-resolution limitations. In agreement with observations, we find that for a sample of major and minor mergers hosting at least one AGN, the fraction harbouring dual AGN is 20–30 and 1–10 per cent, respectively. We quantify the effects of merger mass ratio (0.1 to 1), geometry (coplanar, prograde and retrograde, and inclined), disc gas fraction and BH properties, finding that the mass ratio is the most important factor, with the difference between minor and major mergers varying between factors of a few to orders of magnitude, depending on the luminosity and filter used. We also find that a shallow imaging survey will require very high angular resolution whereas a deep imaging survey will be less resolution-dependent.

DOI: <https://doi.org/10.1093/mnras/stx1067>

Posted at the Zurich Open Repository and Archive, University of Zurich

ZORA URL: <https://doi.org/10.5167/uzh-142897>

Journal Article

Published Version

Originally published at:

Capelo, Pedro R; Dotti, Massimo; Volonteri, Marta; Mayer, Lucio; Bellovary, Jillian M; Shen, Sijing (2017). A survey of dual active galactic nuclei in simulations of galaxy mergers: frequency and properties. *Monthly Notices of the Royal Astronomical Society*, 469(4):4437–4454.

DOI: <https://doi.org/10.1093/mnras/stx1067>

A survey of dual active galactic nuclei in simulations of galaxy mergers: frequency and properties

Pedro R. Capelo,¹★ Massimo Dotti,^{2,3} Marta Volonteri,⁴ Lucio Mayer,¹
Jillian M. Bellovary⁵ and Sijing Shen⁶

¹Center for Theoretical Astrophysics and Cosmology, Institute for Computational Science, University of Zurich, Winterthurerstrasse 190, CH-8057 Zurich, Switzerland

²Dipartimento di Fisica G. Occhialini, Università degli Studi di Milano–Bicocca, Piazza della Scienza 3, I-20126 Milano, Italy

³INFN, Sezione Milano–Bicocca, Piazza della Scienza 3, I-20126 Milano, Italy

⁴Institut d'Astrophysique de Paris, Sorbonne Universités, UPMC Univ. Paris 06 et CNRS, UMR 7095, 98bis boulevard Arago, F-75014 Paris, France

⁵Department of Physics, Queensborough Community College, 222-05 56th Avenue, Bayside, NY 11364, USA

⁶Institute of Astronomy, University of Cambridge, Madingley Road, Cambridge CB3 0HA, UK

Accepted 2017 April 28. Received 2017 April 21; in original form 2016 November 28

ABSTRACT

We investigate the simultaneous triggering of active galactic nuclei (AGN) in merging galaxies, using a large suite of high-resolution hydrodynamical simulations. We compute dual-AGN observability time-scales using bolometric, X-ray and Eddington-ratio thresholds, confirming that dual activity from supermassive black holes (BHs) is generally higher at late pericentric passages, before a merger remnant has formed, especially at high luminosities. For typical minor and major mergers, dual activity lasts ~ 20 – 70 and ~ 100 – 160 Myr, respectively. We also explore the effects of X-ray obscuration from gas, finding that the dual-AGN time decreases at most by a factor of ~ 2 , and of contamination from star formation. Using projected separations and velocity differences rather than three-dimensional quantities can decrease the dual-AGN time-scales by up to ~ 4 , and we apply filters that mimic current observational-resolution limitations. In agreement with observations, we find that for a sample of major and minor mergers hosting at least one AGN, the fraction harbouring dual AGN is ~ 20 – 30 and ~ 1 – 10 per cent, respectively. We quantify the effects of merger mass ratio (0.1 to 1), geometry (coplanar, prograde and retrograde, and inclined), disc gas fraction and BH properties, finding that the mass ratio is the most important factor, with the difference between minor and major mergers varying between factors of a few to orders of magnitude, depending on the luminosity and filter used. We also find that a shallow imaging survey will require very high angular resolution whereas a deep imaging survey will be less resolution-dependent.

Key words: galaxies: active – galaxies: interactions – galaxies: nuclei.

1 INTRODUCTION

A direct consequence of the hierarchical paradigm of structure formation (e.g. Blumenthal et al. 1984) are mergers between galaxies. Since supermassive black holes (BHs) are believed to exist at the centre of most massive galaxies (e.g. Kormendy & Richstone 1995; Ferrarese & Ford 2005), merging systems with two BHs are expected to be common. Moreover, as galaxy mergers can trigger active galactic nuclei (AGN; e.g. Di Matteo, Springel & Hernquist 2005; Hopkins et al. 2006; Younger et al. 2008; Johansson, Burkert & Naab 2009; Hopkins & Quataert 2010; Hayward et al.

2014; Capelo et al. 2015), dual AGN – defined in this paper as systems with two AGN with a separation $0.1 \lesssim d \lesssim 100$ kpc – should also be quite frequent.

Both observations and simulations show that AGN fraction/activity increases with decreasing galaxy separation (e.g. Ellison et al. 2011; Silverman et al. 2011; Koss et al. 2012; Ellison et al. 2013; Capelo et al. 2015), implying that the same should happen with dual-AGN activity. However, even though several dual AGN with separations $\gtrsim 10$ kpc have been detected (e.g. Myers et al. 2008; Hennawi et al. 2010; Liu et al. 2011; Koss et al. 2012), observed dual AGN with separations $\lesssim 10$ kpc are very rare. One reason for this paucity is the inherent difficulty in spatially resolving two AGN at such small separations, especially at redshift $z \gtrsim 0.1$. One of the most promising diagnostics for the existence

* E-mail: pcapelo@physik.uzh.ch

of dual AGN is the presence of double-peaked narrow-line (NL) emission with line-of-sight velocity splitting of $\gtrsim 100 \text{ km s}^{-1}$. Unfortunately, this splitting may be due to a variety of other phenomena, including outflows and rotating discs (see e.g. Komossa & Zensus 2016), giving rise to many negative outcomes (e.g. Tingay & Wayth 2011; Gabányi et al. 2016) and necessitating follow-up observations to confirm the candidates. Hence, only a handful of systems have been so far confirmed (e.g. Fu et al. 2011; Liu et al. 2013; Comerford et al. 2015; Müller-Sánchez et al. 2015).

On the numerical side, there are two main avenues of research. Cosmological simulations (e.g. Steinborn et al. 2016; Tremmel et al. 2016; Volonteri et al. 2016) can produce relatively large numbers of galaxy mergers and systems of multiple BHs and AGN, ideally providing the theoretical counterpart to observations yielding the fraction of dual AGN over the total number of AGN (e.g. Shen et al. 2011). These simulations, however, usually lack the required resolution to reliably follow the dynamics and accretion of BHs. Idealized merger simulations, on the other hand, have the advantage of resolving $< \text{kpc}$ scales, which are extremely important to follow the dynamics of the two BHs (e.g. Van Wassenhove et al. 2014), and of letting one study the effect of merger, galactic, and BH parameters in a controlled environment.

In the context of isolated merger simulations, Van Wassenhove et al. (2012) follow the dynamics and accretion on to the BHs of merging galaxies in three idealized merger simulations (1:2 spiral–spiral, 1:2 elliptical–spiral, and 1:10 spiral–spiral), finding that strong dual-AGN activity occurs during the late stages of the encounters, at separations $< 1\text{--}10 \text{ kpc}$, and that much of the AGN activity in mergers is not simultaneous (see also Blecha, Loeb & Narayan 2013, who simulate the connection between dual-AGN activity and double-peaked NLs).

We build upon the work by Van Wassenhove et al. (2012) by analysing a much larger suite of 12 mergers, studying more initial mass ratios (1:1, 1:2, 1:4, 1:6 and 1:10), disc gas fractions (30 and 60 per cent), and geometries (coplanar, prograde–prograde, retrograde–prograde, prograde–retrograde, and inclined), therefore being able to assess the importance of merger and galactic properties. We also include control runs, in which we study the effects of varying BH properties such as mass and feedback efficiency. In order to better mimic observational limitations, we additionally ‘observe’ our mergers from 100 random lines of sight, study AGN activity with different thresholds (bolometric and X-ray luminosity, and Eddington ratio) and explore the effects of gas obscuration and star formation contamination on X-ray dual-AGN time-scales.

In Sections 2 and 3, we describe the numerical setup of our simulations and the methods of our analysis, respectively. In Section 4, we discuss in detail the results of one of our runs (Section 4.1); explore the effects of obscuration and contamination from star formation (Section 4.2); assess the importance of merger, galactic, and BH parameters (Section 4.3); and compare the results to other theoretical and observational data (Section 4.4). We summarize and conclude in Section 5.

2 NUMERICAL SETUP

In the following, we summarize the setup of the 12 simulated mergers of our suite. We refer the reader to Capelo et al. (2015) for more details on 11 of these mergers (Runs 01–10 and C3 in their table 1) and to Capelo & Dotti (2017) for an additional merger – which here we name C4 for consistency of notation – where we increased the initial mass of the BHs (see below). The main parameters of each merger are shown in Table 1. This suite is a follow-up of a similar

Table 1. Main (initial) simulation parameters for our six major mergers (Runs 01–06), four minor mergers (Runs 07–10), and two control runs (Runs C3–C4). For consistency, we use the same notation as in Capelo et al. (2015), where their Runs C1–C2 had zero BH accretion and therefore are not relevant for the current study. (1) Run number. (2) Mass ratio q_G between the merging galaxies. (3) Angle θ_1 between the primary galaxy’s angular momentum vector and the overall orbital angular momentum vector, in radians. (4) Angle θ_2 between the secondary galaxy’s angular momentum vector and the overall orbital angular momentum vector, in radians. (5) Gas fraction in the galactic disc. (6) BH mass (in units of $2 \times 10^{-3} M_{\text{bulge}}$). (7) BH feedback efficiency ϵ_f .

Run	q_G	θ_1	θ_2	gas	M_{BH}	ϵ_f
01	1:1	0	0	0.3	1	0.001
02	1:2	0	0	0.3	1	0.001
03	1:2	$\pi/4$	0	0.3	1	0.001
04	1:2	π	0	0.3	1	0.001
05	1:2	0	π	0.3	1	0.001
06	1:2	0	0	0.6	1	0.001
07	1:4	0	0	0.3	1	0.001
08	1:4	$\pi/4$	0	0.3	1	0.001
09	1:6	0	0	0.3	1	0.001
10	1:10	0	0	0.3	1	0.001
C3	1:2	0	0	0.3	1	0.005
C4	1:2	0	0	0.3	2.5	0.001

suite of mergers (Callegari et al. 2009, 2011; Van Wassenhove et al. 2012, 2014), initially constructed to study the pairing time-scales of BHs in unequal-mass galaxy mergers (see also Pfister et al. 2017).

We simulate isolated mergers of disc galaxies at $z = 3$, initially at a distance equal to the sum of their virial radii, set on parabolic orbits (Benson 2005) with a first pericentric distance equal to 20 per cent of the virial radius of the larger (‘primary’) galaxy (Khochfar & Burkert 2006), which is the same for all encounters. Whereas the global orbital parameters are identical for all the mergers in the suite,¹ the internal orbital parameters are not: we include coplanar, prograde–prograde, retrograde–prograde, and prograde–retrograde encounters, and inclined mergers, by varying the angle (0, $\pi/4$ or π radians) between the initial individual galactic angular momentum vector of each galaxy and the global angular momentum vector.

All galaxies are composed of a dark matter halo, a stellar and gaseous disc, a stellar bulge, and a central BH. The dark matter halo is described by a Navarro–Frenk–White (NFW; Navarro, Frenk & White 1996) profile with spin and concentration parameters 0.04 and 3, respectively, up to the virial radius, and by an exponentially decaying NFW profile for larger radii (Springel & White 1999). The disc is described by an exponential disc with an isothermal sheet (Spitzer 1942; Camm 1950), with its mass, equal to 4 per cent of the virial mass of the galaxy, divided into gas (30 or 60 per cent, depending on the merger) and stars. The initial value of the disc scale radius, r_{disc} , comes from imposing conservation of specific angular momentum of the material that forms the disc, whereas the initial disc scale height, z_{disc} , is set equal to 10 per cent of r_{disc} . The bulge is described by a spherical Hernquist (1990) profile with a mass (M_{bulge}) and scale radius equal to 0.8 per cent of the virial mass of the galaxy and 20 per cent of r_{disc} , respectively. The primary galaxy in each merger has an initial virial mass of $2.21 \times 10^{11} M_{\odot}$, whereas the secondary galaxy has a mass that is a fraction (1/10,

¹ Ignoring the fact that the sum of the virial radii changes with the initial mass ratio, since the smaller (‘secondary’) galaxy varies.

1/6 and 1/4 in the case of ‘minor’ mergers; 1/2 and 1 in the case of ‘major’ mergers) of that of the larger galaxy. The initial disc scale radius varies from 0.53 kpc (for the secondary galaxy in the 1:10 merger) to 1.13 kpc (for the primary galaxy in all mergers).

The central BH has a mass M_{BH} proportional to that of the stellar bulge (Marconi & Hunt 2003), where the constant of proportionality is 2×10^{-3} (‘standard’) for all mergers except for one (Run C4; Capelo & Dotti 2017), in which we instead use 5×10^{-3} (‘large’), as it was recently shown that the BH–bulge relation might evolve with redshift (Merloni et al. 2010). BHs are sink particles that accrete preferentially nearby, cold and dense gas (Bellovary et al. 2010), according to a Bondi–Lyttleton–Hoyle (hereafter, Bondi; Bondi 1952; Bondi & Hoyle 1944; Hoyle & Lyttleton 1939) formula:²

$$\dot{M}_{\text{BH}} = \frac{4\pi\alpha M_{\text{BH}}^2 \rho}{(c_s^2 + v^2)^{3/2}}, \quad (1)$$

where ρ is the local gas density, c_s is the local sound speed, v is the relative velocity between gas and BH, G is the gravitational constant and α is a boost factor.³ Accretion is then capped at mildly super-Eddington values, by limiting $f_{\text{Edd}} \equiv \dot{M}_{\text{BH}}/\dot{M}_{\text{BH, Edd}}$ at α , where

$$\dot{M}_{\text{BH, Edd}} = \frac{4\pi G M_{\text{BH}} m_p}{\epsilon_r \sigma_T c}, \quad (2)$$

where m_p is the proton mass, σ_T is the Thomson cross-section, c is the speed of light in vacuum and $\epsilon_r = 0.1$ (Shakura & Sunyaev 1973) is the radiative efficiency. The latter gives the fraction of BH accretion energy rate ($\dot{M}_{\text{BH}} c^2$) that is emitted as radiation: $L_{\text{bol}} = \epsilon_r \dot{M}_{\text{BH}} c^2$. Part of this radiation is then coupled to the gas, in the form of thermal energy (Bellovary et al. 2010). The amount of coupling is set by the BH feedback efficiency parameter ϵ_f , which is equal to 0.001 (‘standard’) in all runs except for one of the control runs (Run C3), in which $\epsilon_f = 0.005$ (‘high’).

All 12 simulations were performed with the N -body smoothed particle hydrodynamics (SPH) code GASOLINE (Wadsley, Stadel & Quinn 2004) – an extension of PKDGRAV (Stadel 2001) – which has realistic implementations of line cooling for atomic hydrogen and helium, and metals (Shen, Wadsley & Stinson 2010); star formation (stars can stochastically form with a star formation efficiency of 0.015 from gas colder than 6000 K and denser than 100 a.m.u. cm^{-3}), supernova feedback, and stellar winds (Stinson et al. 2006); and the above-mentioned recipe for BH accretion and feedback (Bellovary et al. 2010). No additional corrections (such as an over-pressurized equation of state; e.g. Springel & Hernquist 2003) to the gas thermodynamics were adopted. The star formation density threshold was chosen to be near the maximum density at which the Jeans mass (M_{Jeans}) of gas at the temperature floor of the simulations (T_{floor}) is resolved by N particles:

$$n_{\text{max}} = C \left(\frac{T_{\text{floor}}}{200 \text{ K}} \right)^3 \left(\frac{N}{64} \right)^{-2} \left(\frac{m_{\text{gas}}}{10^3 M_{\odot}} \right)^{-2} \text{ cm}^{-3}, \quad (3)$$

² At each time-step dt , in case of an accretion event, the code takes a quantity dm from the gas, according to the Bondi formula, and adds the same amount to the mass of the BH, therefore neglecting the radiative efficiency and introducing a 10 per cent error.

³ Our standard boost factor is $\alpha = 3$ as originally reported in Capelo et al. (2015), but we recently found that, in some segments of some simulations, the boost factor is doubled (Gabor et al. 2016). Since BH growth is self-regulated by AGN feedback in these simulations, our results are insensitive to the exact value of the boost factor. We partially re-ran one merger simulation with different values of the boost factor (varying it between 1 and 6) and found no significant differences in the BH accretion levels.

where m_{gas} is the gas particle mass and $C \simeq 179$.⁴ In our simulations, $T_{\text{floor}} = 500 \text{ K}$, and we require $N = 64$.

The particle mass of the stellar, gas and dark matter particles is 3.3×10^3 , 4.6×10^3 and $5\text{--}11 \times 10^4 M_{\odot}$, respectively. The gravitational softening, for the same particle types, is 10, 20 and 23–30 pc, respectively (and that of BHs is 5 pc). The range in the dark matter quantities is due to the fact that we want to ensure that the dark matter particles have a mass smaller than 15 per cent of that of the smaller BH in each merger, thus successfully limiting excursions of BHs from the centre of each galaxy. For this reason, we do not need to artificially model unresolved dynamical friction (see e.g. Tremmel et al. 2015 and references therein). All the parameters described here are summarized in tables 1 and 2 of Capelo et al. (2015), which the reader should refer to for more details.

3 ANALYSIS

Consistently with the previous work (Capelo et al. 2015), we divide the encounter in three distinct stages: the ‘stochastic stage’, from the beginning of the simulation to the second pericentric passage; the ‘merger stage’, which ends when the specific angular momentum of the central gas ceases its dramatic oscillations caused by the encounter; and the ‘remnant stage’, which ends when the BH separation (averaged over 5 Myr) is below twice the gravitational softening of the BHs (i.e. the stellar gravitational softening: 10 pc).⁵ After this point, we cannot study reliably the dynamics of the two BHs, due to resolution limitations. Depending on the merger, there are cases when the last stage is fairly short (e.g. Run 02: 0.1 Gyr; see Section 4.1) and cases when it is long (e.g. Run 05, the 1:2 coplanar, retrograde–prograde merger, and Run 08, the 1:4 inclined–primary merger: 0.5 and 1 Gyr, respectively).

Since we are interested in the observability of dual activity, we ‘observe’ the same encounter from several random lines of sight and translate three-dimensional (3D) quantities into projected (on to the plane perpendicular to the line of sight) BH separations (r) and projected (on to the line of sight) BH velocity differences (v). More specifically, the code returns the mass, bolometric luminosity, 3D separation and 3D velocity difference of the BHs every $\Delta t = 0.1 \text{ Myr}$, which is comparable to the characteristic dynamical times in proximity of the BHs (given the BH masses and gravitational softenings involved). We then project the 3D properties on to N random and isotropically distributed lines of sight, where $N = 10$, 100 or 1000. The fraction of projections that results into an either spatial or spectroscopic AGN pair corresponds to the probability p

⁴ This value was obtained using the following definition: $M_{\text{Jeans}} = (\pi^{5/2}/6)[\gamma k_B T/(\mu m_H G)]^{3/2} \rho^{-1/2}$, where k_B is the Boltzmann constant, m_H is the hydrogen mass, and ρ , T , $\gamma = 5/3$ and $\mu \simeq 0.6$ are the mass density, temperature, adiabatic index and mean molecular weight of the gas, respectively. Using an alternative definition, $M_{\text{Jeans}} = [10k_B T/(3(\gamma - 1)\mu m_H G)]^{3/2} (4\pi\rho/3)^{-1/2}$, we obtain $C \simeq 136$.

⁵ In one case in our suite (1:1 merger – Run 01), the 10-pc threshold is reached slightly before the end of the merger stage (as opposed to after, as in all other mergers). For consistency with the other mergers, in this case we decided not to change the length of the merger stage, since the difference in time is minimal. In another case (1:4 inclined–primary merger – Run 08), we stopped the simulation when the remnant stage was as long as the stochastic stage, since the 10-pc threshold had not been reached yet. We note that we have also computed dual-activity observability time-scales considering a much longer remnant stage (i.e. always as long as the stochastic stage, regardless of the 10-pc limit, as in Capelo et al. 2015) and found that, for typical imaging and spectroscopy resolutions, there is no significant change.

of detecting dual AGN, and the expected dual-activity time within Δt is estimated as $\Delta t \times p$. For the remainder of this paper, we use $N = 100$ (see Section A for more details).

Throughout the paper, we adopt different thresholds for bolometric luminosity (from 10^{42} to 10^{44} erg s $^{-1}$) and for X-ray luminosity in the 2–10 keV band (from $10^{41.3}$ to $10^{43.3}$ erg s $^{-1}$). Note that the secondary BHs in the stochastic stages of the minor mergers (mass ratios 1:4, 1:6 and 1:10) cannot reach the highest X-ray threshold we consider ($10^{43.3}$ erg s $^{-1}$). We also assume typical thresholds of 1 and 10 kpc (for imaging), and 150 km s $^{-1}$, as the minimum velocity difference needed to separate two AGN in spectroscopic observations.

4 RESULTS

We first study the dual-activity observability time-scales for one individual merger (Section 4.1) and discuss the effects of obscuration caused by intervening gas in the host galaxy (Section 4.2). We then compare the results of all encounters (Section 4.3) to assess the effects of merger (mass ratio, geometry) or galactic parameters (gas fraction) and of BH-related quantities (BH mass, feedback efficiency). Finally, we compare our results to those from observational surveys and theoretical studies (Section 4.4).

4.1 The default merger

The ‘default merger’ (Run 02 in Tables 1–2) is the 1:2 coplanar, prograde–prograde merger with 30 per cent gas fraction and standard BH mass and feedback efficiency. We chose this encounter because it is at the intersection of most of our parameter-space studies (see Section 4.3).

4.1.1 General behaviour

In Fig. 1, we show the detailed history of the default merger. In the top two panels, we show the (3D) separation and velocity difference between the two BHs, as a function of time. In the remainder of this paper, unless otherwise stated, we use projected quantities, as explained in Section 3. In the bottom panel, we show the BH accretion rate (and bolometric luminosity) of the two BHs. This figure allows one to appreciate that, based on 3D quantities, spectroscopic searches for large velocity differences should identify for the most part dual AGN at the first pericentre, when their separation is 10–20 kpc, where BHs spend a large amount of time with sufficiently large velocity difference, and also at subsequent pericentres, but for much shorter-lived episodes at higher velocities. Conversely, searches for physically distinct nuclei would be more successful at finding AGN at apocentres. As shown in the bottom panel, this has to be, however, convolved with the AGN luminosities and reassessed taking projection effects into account. Projecting a vector on to a random line of sight (what we do for velocity differences) or on to the plane perpendicular to such line of sight (what we do for separations) has vastly different results. The probability distribution of projected velocity differences is flat between 0 and the 3D value. On the other hand, the probability distribution of projected separations peaks at the 3D separation, with the probability of having small projected separations being very small (see Fig. A1).

In order to understand better the dual-activity results presented later, we first show in Fig. 2 the orbital history of the encounter in a complementary way, by computing the time spent *above* a given r or v . We also consider the results on a stage-by-stage basis, in order

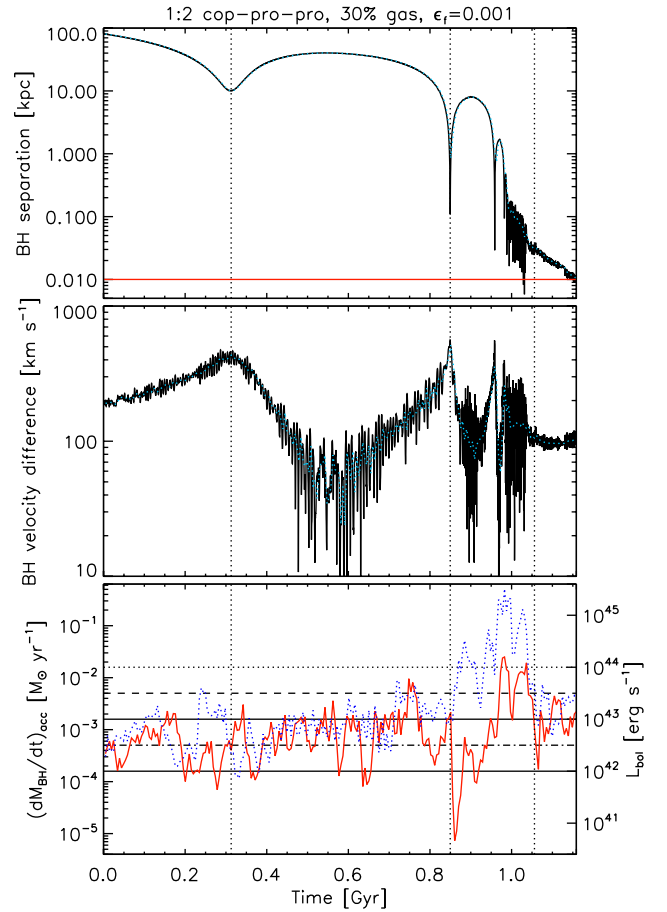


Figure 1. Temporal evolution of the 1:2 coplanar, prograde–prograde merger with 30 per cent gas fraction and standard BH mass and feedback efficiency (the default merger; total encounter time 1.158 Gyr), from the beginning of the stochastic stage to the end of the remnant stage. In all panels, the vertical, dotted and black lines show, from left to right: (i) the first pericentric passage, (ii) the end of the stochastic stage and (iii) the end of the merger stage. Top panel: 3D separation between the two BHs, shown every 0.1 Myr (black, solid), together with its average every 5 Myr (cyan, dot). The horizontal, solid and red line shows the stellar gravitational softening (10 pc). Middle panel: 3D velocity difference between the two BHs, shown every 0.1 Myr (black, solid), together with its average every 5 Myr (cyan, dot). Bottom panel: BH accretion rate (and bolometric luminosity) of the primary (blue, dot) and secondary (red, solid) BH, averaged every 5 Myr. The horizontal lines show different levels of bolometric luminosity, between 10^{42} and 10^{44} erg s $^{-1}$ [the line styles match those of Figs 3 (left panels), 6, A2, B1–B2, and B4–B8].

to more easily interpret the importance of each phase for the dual-activity time-scales. The stochastic stage (total time 0.849 Gyr) is clearly the dominant stage for all r and all v , except at very high v , when the time spent during the merger stage (total time 0.206 Gyr) is comparable. The remnant stage (total time 0.103 Gyr), on the other hand, is never visible in the r -panel (because the largest separation during such stage is <0.1 kpc) and negligible in the v -panel (especially for $v \gtrsim 100$ km s $^{-1}$, the typical range for spectroscopy surveys).

4.1.2 Dual activity

In Fig. 3, we show the amount of time the two BHs spend *above* a given r or v when they accrete above a given threshold

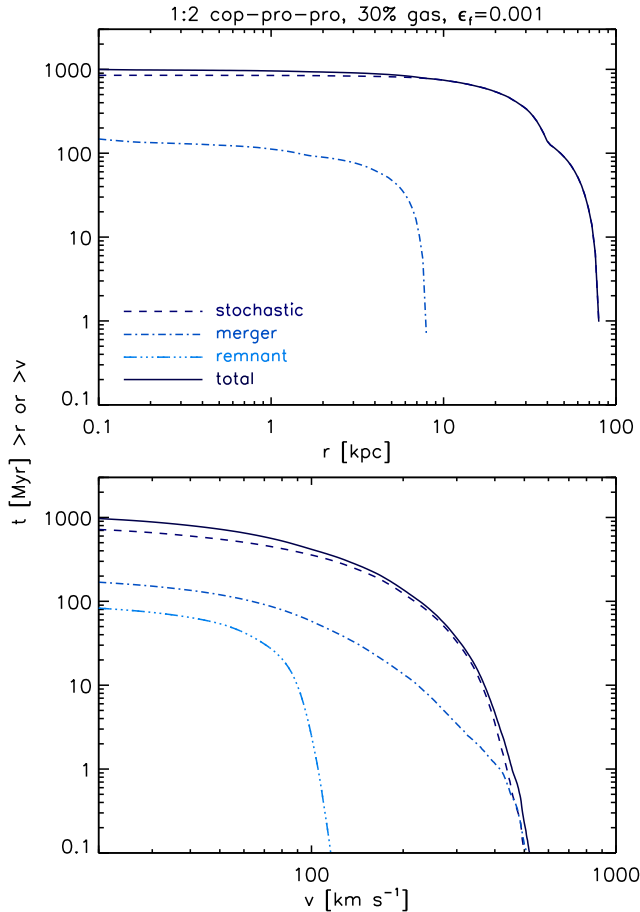


Figure 2. For the default merger: time spent *above* a given projected separation (top panel) and projected velocity difference (bottom panel) between the two BHs, during the stochastic stage (dash), the merger stage (dash-dot), the remnant stage (dash-triple-dot) and the entire encounter (solid). The remnant stage is actually never visible in the r -panel, because the BH projected separation during such stage is always lower than 0.1 kpc, and is negligible in the v -panel.

(bolometric – L_{bol} – or hard-X-ray – $L_{2-10\text{keV}}$ – luminosity, or Eddington ratio – f_{Edd}). We show it in a ‘cumulative’ way (time spent *above* r or v , rather than time spent *at* r or v) to highlight the dependence on any *minimum* projected separation or velocity difference, to mimic observational limitations. To calculate the X-ray time-scales, we applied a simple inverse bolometric correction (Hopkins, Richards & Hernquist 2007): $L_{2-10\text{keV}} = L_{\text{bol}}[c_1(L_{\text{bol}}/10^{10}L_{\odot})^{k_1} + c_2(L_{\text{bol}}/10^{10}L_{\odot})^{k_2}]^{-1}$, where $c_1 = 10.83$, $k_1 = 0.28$, $c_2 = 6.08$ and $k_2 = -0.02$. The solid line in the bolometric and X-ray panels represents what is typically used as the threshold for AGN activity: 10^{43} (i.e. $2.6 \times 10^9 L_{\odot}$; e.g. Steinborn et al. 2016) and $10^{42.3}$ erg s $^{-1}$ (e.g. Silverman et al. 2011), respectively.

The dual-activity curves at low luminosity thresholds (e.g. $L_{\text{bol}} = 10^{42}$ erg s $^{-1}$ or $L_{2-10\text{keV}} = 10^{41.3}$ erg s $^{-1}$) follow the orbital history of the encounter (compare with Fig. 2). This is because, at low thresholds, the BHs are both active for a significant fraction of the encounter. When the threshold increases, the dual-activity time obviously decreases, but also ceases to follow the orbital history. Activity (and especially simultaneous activity) is high only during the merger stage, when gas gets efficiently funnelled into the central regions of the galaxies due to tidal torques and/or ram-pressure shocks (Capelo & Dotti 2017). During the initial part of the merger

stage (i.e. between the second and third pericentric passages), only the primary BH is active (see Fig. 1). This is the reason why, at e.g. $L_{\text{bol}} = 10^{43.5}$ erg s $^{-1}$ or $L_{2-10\text{keV}} = 10^{42.3}$ erg s $^{-1}$, we see a break in the dual-activity curves at $r \sim 2$ kpc, which is the separation at third apocentre, rather than at ~ 8 kpc (second apocentre).

If we consider a typical bolometric threshold for AGN activity (10^{43} erg s $^{-1}$) and typical thresholds for resolving dual AGN in imaging (1 and 10 kpc) and spectroscopy (150 km s $^{-1}$), we obtain a dual-activity observability time-scale equal to 3.7, 2.3 and 1.0 per cent, respectively, of the total encounter time (see Run 02 in Table 2). These fractions increase to 4.4, 3.7 and 4.5 per cent when we divide the dual-activity time by the time spent above those separations and velocity differences (which can be compared to theoretical results from cosmological simulations that provide the number of dual AGN out of the total number of BH pairs – see Section 4.4.2). The numbers increase further, to 12.5, 12.7 and 14.1 per cent, when we consider the dual-activity time divided by the activity time, defined as the time when at least one of the BHs is active, spent above those r and v : the proper comparison, in this case, is to observational results that provide the number of dual AGN out of the total number of pairs in which there is at least one AGN (see Section 4.4.1).

In Fig. 4, the dual-activity time is shown as a function of two variables, chosen from r , v and $L_{\text{bol},1}/L_{\text{bol},2}$ (we note that *only* in this figure we show the dual-activity time *at* r and/or v , rather than *above* r and/or v). The top three panels (in each group of six panels) show the bolometric-luminosity ratio between the two active BHs, as a function of projected separation. This ratio can be as high as 10^3 , but only at small separations ($r \lesssim 2$ kpc), when the two galaxies are likely interacting. At larger separations ($r \gtrsim 8$ kpc), when the two galaxies are mostly isolated, activity is much lower. This means that, in case both BHs are active, they are likely to be barely active (i.e. their luminosity is just above the given threshold), which is the reason why the bolometric-luminosity ratio is close to unity (and approaches unity with increasing r). Overall, the ratio is more often above unity than below: the primary, more massive BH is on average more luminous than the secondary (see Capelo et al. 2015 for more discussion on this). The ‘cloud’ of dual activity around ~ 20 – 40 kpc is simply due to the fact that the BHs spend a large amount of time at that distance during the first apocentre.

The BHs are active mostly when their projected velocity difference is $v \lesssim 150$ km s $^{-1}$. These results are given for projected quantities, as opposed to 3D quantities. The time-scales do in fact change quite significantly, especially when filtering by v , and we quantify it in Section A (see Figs A2–A3).

4.2 X-ray obscuration and dilution

The results described in the previous section assume that the intrinsic luminosity is affected for the observer only by distance dimming. In reality, observations at optical or X-ray wavelengths are also affected by dimming caused by intervening dust or gas, as well as contamination from stellar sources, stars or X-ray binaries in optical or X-ray, respectively. In this paper, we discuss only X-ray luminosities, therefore we will consider (i) the obscuration produced by the gas surrounding the BH and (ii) the contamination (or dilution) from X-ray binaries.

Here we neglect the contribution of the Milky Way’s interstellar medium and of the intergalactic medium. We also neglect obscuration in the vicinity of the BH (torus or broad-line region), below our resolution, as the correction is statistical, i.e. it depends on the inclination with respect to the line of sight and is not related to

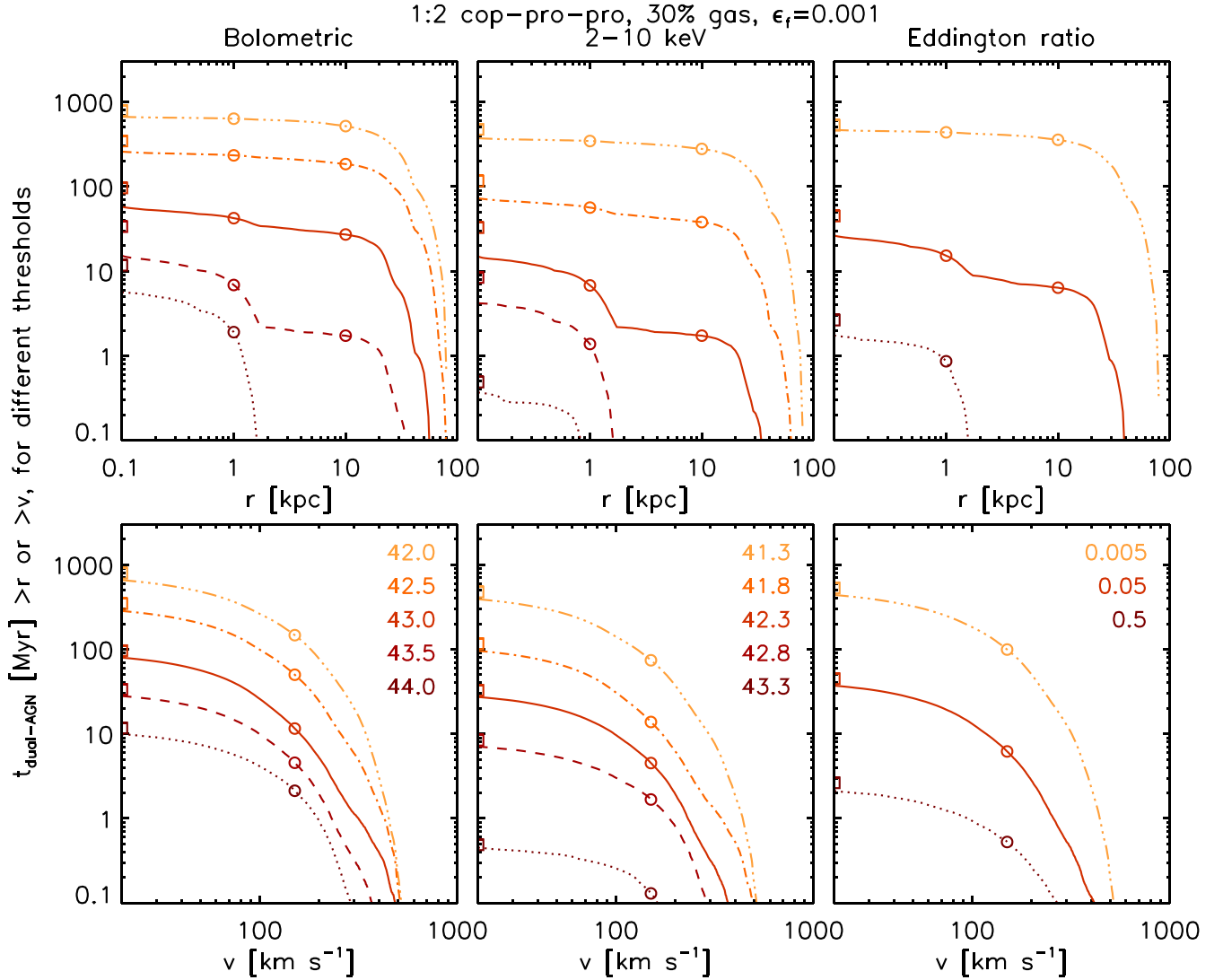


Figure 3. For the default merger: dual-activity time *above* a given projected separation (top panels) and projected velocity difference (bottom panels) between the two BHs, for several bolometric [left panels; 10⁴² (dash-triple-dot), 10^{42.5} (dash-dot), 10⁴³ (solid), 10^{43.5} (dash) and 10⁴⁴ (dot) erg s⁻¹], 2–10 keV [middle panels; 10^{41.3} (dash-triple-dot), 10^{41.8} (dash-dot), 10^{42.3} (solid), 10^{42.8} (dash) and 10^{43.3} (dot) erg s⁻¹], and Eddington-ratio [right panels; 0.005 (dash-triple-dot), 0.05 (solid) and 0.5 (dot)] thresholds. The squares indicate the dual-activity time regardless of any r or v filter (i.e. $r = v = 0$). The circles refer to the following projected separations and velocity differences: 1 and 10 kpc and 150 km s⁻¹ (see Table B1). The breaks visible in the upper panels occur when the BHs are at apocentre, i.e. when the BHs spend a relatively large amount of time (e.g. the break clearly visible at ~ 2 kpc is due to the third apocentric passage at ~ 0.96 Gyr; see Fig. 1). Similar figures, for all other mergers, can be found in the online-only material.

properties of the merger. We focus instead on the role of the gas belonging to the BHs' hosts, which is expected to screen the AGN differently during the merger.

The column density, N_{H} , can obviously vary wildly during the encounter and is also dependent on the line of sight: the central BH of an isolated galaxy viewed face-on will be less obscured than that in a merging galaxy viewed edge-on. Since here we are interested only in order-of-magnitude estimates, we consider one typical column density per BH per time-step (i.e. every 5 Myr, the frequency of the main outputs). To obtain these values, we first compute the average face-on column density by calculating the total gas mass inside a cylinder of radius $R_{\text{cyl}} = 0.1$ kpc (five times the gas gravitational softening), whose axis is parallel to the z -axis and includes the position of the BH, between the BH itself and the observer (at infinity). Thus, we have two masses (one per direction: $+z$ and $-z$), which we average. We then divide this average mass

by $\mu m_{\text{H}} S$, where $S = \pi R_{\text{cyl}}^2$, to obtain the face-on column density. We do the same for the edge-on column density, this time averaging four different gas masses, using cylinders with their axes parallel to the x and y axes. At the beginning of the stochastic stage, we obtain a column density of $\sim 3 \times 10^{22}$ and $\sim 4 \times 10^{23}$ cm⁻², for the primary BH's face-on and edge-on case, respectively, which is very close to what is expected analytically from the initial conditions (the factor of ~ 10 difference comes from the factor of 10 between r_{disc} and z_{disc}). We computed the same quantities in the case when BHs do not accrete (Run C1 in Capelo et al. 2015), to check for dependency on BH accretion and feedback, and obtained similar values. Finally, we average the two column densities (face-on and edge-on) to obtain a typical column density N_{H} for each BH every 5 Myr. We find that N_{H} is always very close to 10²³ cm⁻² during the stochastic and remnant stages and within less than one order of magnitude from such value during the merger stage. We computed

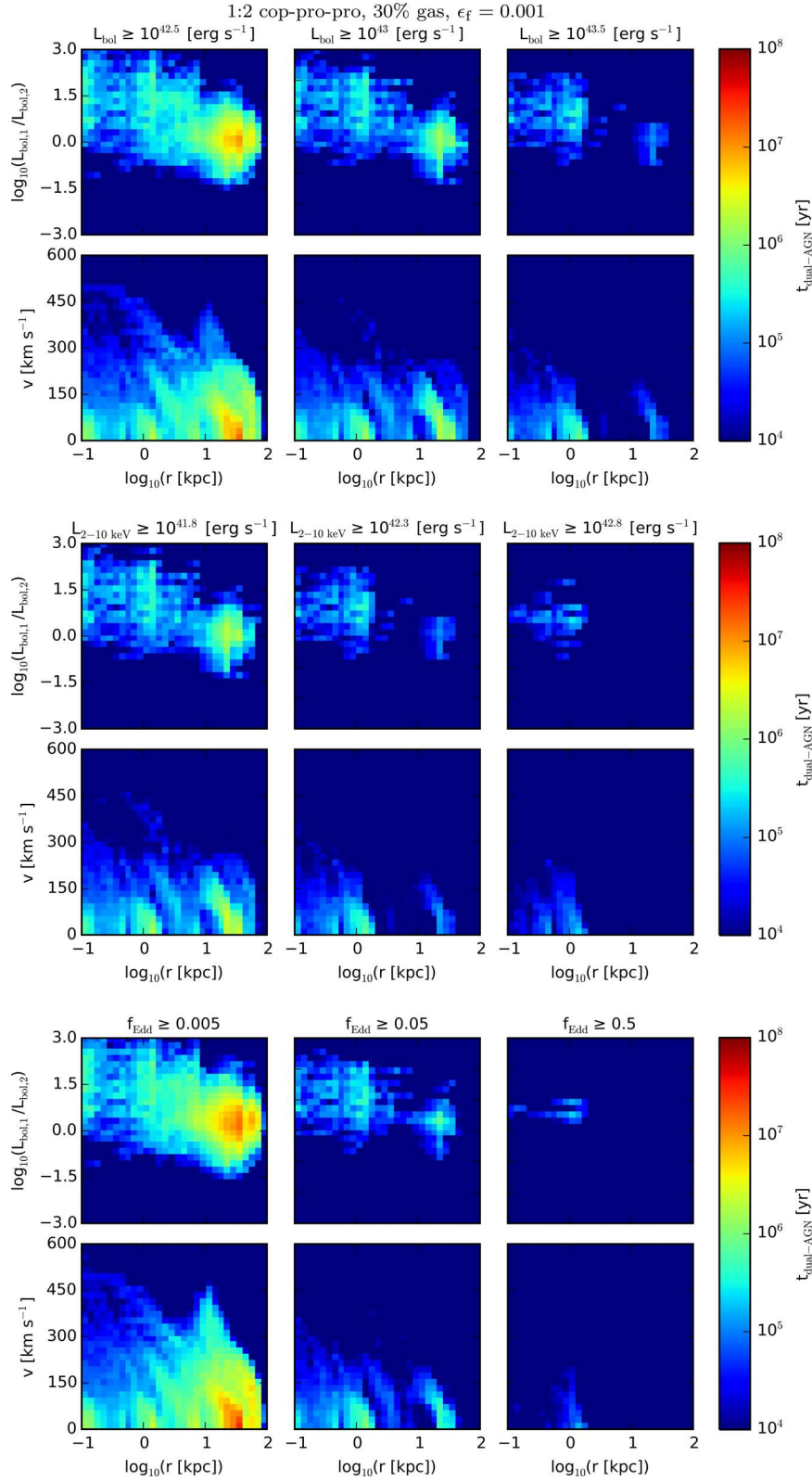


Figure 4. For the default merger: dual-activity time as a function of projected separation and velocity difference, and bolometric-luminosity ratio between the two BHs, for three bolometric [top six panels; $10^{42.5}$ (left), 10^{43} (centre) and $10^{43.5}$ (right) erg s^{-1}], 2–10 keV [middle six panels; $10^{41.8}$ (left), $10^{42.3}$ (centre) and $10^{42.8}$ (right) erg s^{-1}], and Eddington-ratio [bottom six panels; 0.005 (left), 0.05 (centre) and 0.5 (right)] thresholds. Each side is divided in 30 bins [$\Delta \log_{10}(r \text{ [kpc]}) = 0.1$, $\Delta v = 20 \text{ km s}^{-1}$ and $\Delta \log_{10}(L_{\text{bol},1}/L_{\text{bol},2}) = 0.2$]. Similar figures, for all other mergers, can be found in the online-only material.

the same quantities also for the merger with 60 per cent gas fraction (Run 06 in Tables 1–2) and found similar values. The values for the secondary BH are very similar to those of the primary BH, as expected, since the (analytical) column density ratio is proportional to the cube root of the mass ratio. We believe that the little variation in column density, compared, e.g. to that found in Hopkins et al. (2012), is due to the relatively coarser resolution of our simulations.

Using the online tool `WEBPIMMS`,⁶ we calculated the detection factor, f_{through} , defined as the fraction of detected over unabsorbed flux. We considered two redshifts: $z = 3$, since our galaxies are constructed as typical of that redshift (case A), and $z = 0$, in which our galaxies are representative of relatively small, gas-rich local galaxies (case B). The obscuration for case A is almost negligible, whereas for case B it produces a change in the dual-activity time-scales of a factor ~ 2 , more prominent at high thresholds (Fig. 5). We note that these calculations were done for the 2–10 keV band. Observations with harder X-rays (i.e. higher energy) would be less obscured, and vice versa (see e.g. Koss et al. 2016).

Amongst the many other galactic sources of X-rays, the dominant source is the population of high-mass X-ray binaries (HMXB). Since high-mass stars are short-lived, X-ray binaries follow closely the star formation rate (SFR): $L_{\text{HMXB}} = 6.7 \times 10^{39} \times \text{SFR} [\text{M}_{\odot} \text{ yr}^{-1}] \text{ erg s}^{-1}$ (Grimm, Gilfanov & Sunyaev 2003). Since the global SFR in our systems never exceeds $\sim 20 \text{ M}_{\odot} \text{ yr}^{-1}$ (Capelo et al. 2015; Volonteri et al. 2015a,b), the X-ray luminosity from the stellar component is always $< 1.3 \times 10^{41} \text{ erg s}^{-1}$ and reaches such values only for brief bursts during the merger stage. This is one order of magnitude lower than the typical X-ray threshold ($10^{42.3} \text{ erg s}^{-1}$) used to define AGN activity. Hence, contamination from X-ray binaries is negligible.

4.3 Dependence on merger properties

In this section, we study the dependence of the dual-activity observability time on several parameters of both galaxies and mergers, namely the initial mass ratio of the merger, the initial geometry, the initial gas fraction and, mostly for control reasons, the BH mass and feedback efficiency. We focus on the relative differences, to highlight the effects of the above-mentioned parameters, rather than on the absolute results, which are instead the focus of Section 4.4, where we compare our data to other theoretical and observational work. The conclusions in this section should be affected neither by the specifics of the initial conditions nor by the sub-grid recipes (e.g. disc and bulge mass fraction; star formation recipe), since they are kept the same in this parameter study.

4.3.1 Initial mass ratio

The mass ratio is likely the most important factor in determining BH activity. As already shown in Capelo et al. (2015), the smaller (secondary) galaxy always responds strongly to the interaction (mostly during the merger stage), regardless of the initial mass ratio. On the other hand, the larger (primary) galaxy is affected in different

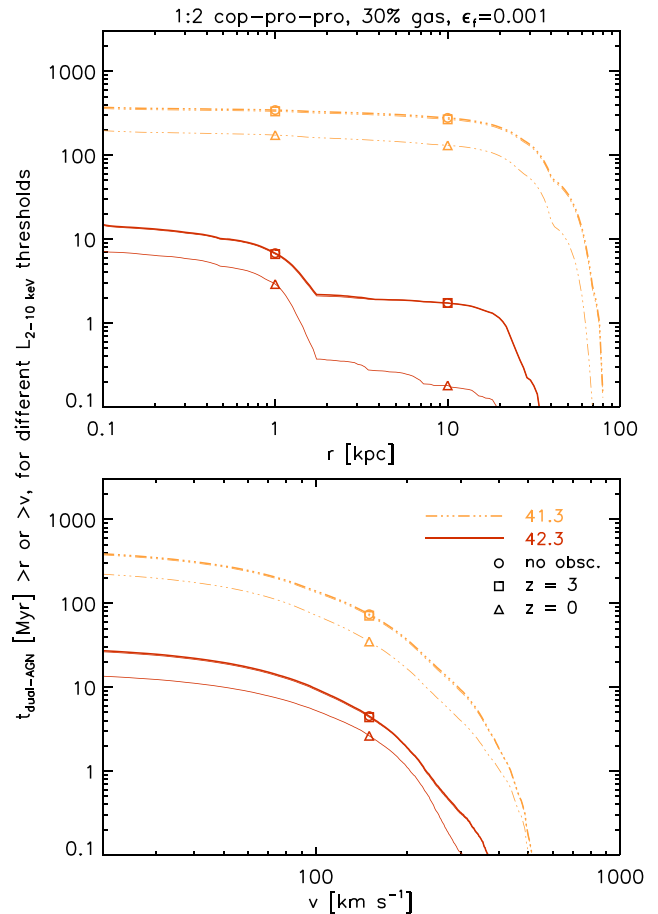


Figure 5. For the default merger: dual-activity time above a given projected separation (top panel) and projected velocity difference (bottom panel) between the two BHs, for two 2–10 keV thresholds [$10^{41.3}$ (dash-triple-dot) and $10^{42.3}$ (solid) erg s^{-1}]. The symbols refer to the following projected separations and velocity differences: 1 and 10 kpc and 150 km s^{-1} . For each luminosity threshold, we show three cases: the system is not obscured (thick lines and circles; same as the middle panels of Fig. 3); the system is obscured and assumed to be at $z = 3$ (case A; thin lines and squares); and the system is obscured and assumed to be at $z = 0$ (case B; thin lines and triangles). Case A is almost not visible, as it is almost indistinguishable from the case with no obscuration.

ways depending on the mass of the secondary. In minor mergers, the primary BH shows almost no response, because the secondary galaxy is too little to produce any significant effects (in other words, the primary galaxy is almost ‘unaware’ of the interaction). In major mergers, instead, the companion is large enough to significantly affect the primary and produce higher levels of primary BH activity.

In Fig. 6, we show the dual-activity time above a given projected separation, divided by the activity time above the same r , for all five coplanar, prograde–prograde mergers with 30 per cent gas fraction and standard BH mass and feedback efficiency, which have initial mass ratios ranging from 1 to 0.1 (Runs 01, 02, 07, 09 and 10 in Tables 1–2). The trend with mass ratio is as expected: major mergers are more active than minor mergers.⁷ We can quantify the

⁷ The trend is the same also in the v case (not shown in the paper). In case we do not normalize, the longer duration of the minor mergers is not sufficient to offset their intrinsically low levels of activity, except at low thresholds (see Fig. B4).

⁶ <https://heasarc.gsfc.nasa.gov/Tools/w3pimms.html> (powered by PIMMS version 4.8d; Mukai 1993). The settings used are the following: Convert from ‘Unabsorbed Flux’ into ‘Flux’; Input Energy Range = Output Energy Range = 2–10 keV; Galactic $N_{\text{H}} = 0.0$; Power Law with Photon Index = 1.8 (the same used in our inverse bolometric correction; Hopkins et al. 2007); redshift = 0 or 3. Intrinsic N_{H} was computed from the outputs. For $N_{\text{H}} = 10^{23} \text{ cm}^{-2}$: $f_{\text{through}} = 0.559$ and 0.965 , for $z = 0$ and 3 , respectively.

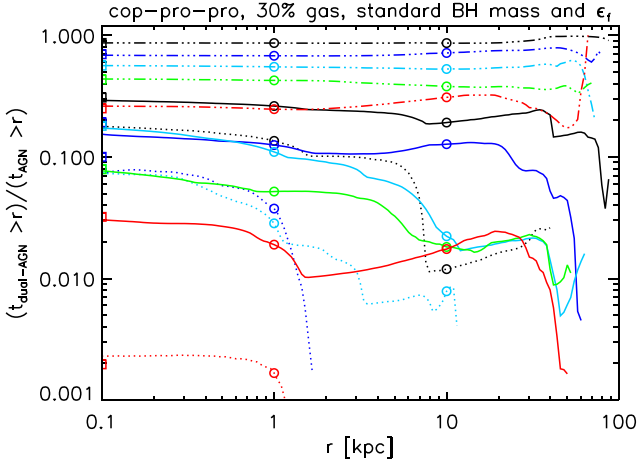


Figure 6. Dual-activity time above a given projected separation between the two BHs, divided by the activity time above the same r , using three bolometric thresholds [10^{42} (dash-triple-dot), 10^{43} (solid) and 10^{44} (dot) erg s^{-1}], for the coplanar, prograde–prograde mergers with 30 per cent gas fraction, standard BH mass and feedback efficiency, and different mass ratios (1:1: black, total encounter time 0.978 Gyr; 1:2: blue, 1.158 Gyr; 1:4: cyan, 1.271 Gyr; 1:6: green, 1.682 Gyr; and 1:10: red, 3.305 Gyr). The squares and circles refer to the following projected separations: 0, 1 and 10 kpc. The seemingly random behaviour of the curves at high r is due to statistical fluctuations, as the time spent at those high projected separations is relatively low (see Fig. 2). At $r = 1$ kpc, the normalized dual-activity time is highest for the 1:1 merger, followed by the 1:2, 1:4, 1:6 and 1:10 mergers, regardless of the luminosity threshold shown (except for $L_{\text{thr}} = 10^{44} \text{ erg s}^{-1}$, when the 1:6 merger is not visible).

ratio of normalized dual-activity time between major and minor mergers, which ranges from factors of a few at $10^{42} \text{ erg s}^{-1}$ to ~ 10 at $10^{43} \text{ erg s}^{-1}$, to $\gg 10$ at $10^{44} \text{ erg s}^{-1}$.

Fig. 6 highlights an important result. At low luminosity thresholds ($< 10^{43} \text{ erg s}^{-1}$) the curves are mostly flat, i.e. independent of r . Conversely, at high luminosity thresholds ($10^{44} \text{ erg s}^{-1}$) dual activity is captured only at small r , when BHs are most active, albeit for short times. The prediction is that, in order to identify dual AGN, shallow surveys will be more affected by an increase of angular resolution, with respect to deeper surveys.

In Fig. 7, we show again the normalized time (for $r = 1$ and 10 kpc and for $v = 150 \text{ km s}^{-1}$) for the five mergers of this section,

Table 2. Dual-activity observability time-scales for all mergers (numbered as in Table 1), assuming a threshold $L_{\text{bol}} = 10^{43} \text{ erg s}^{-1}$ and using different imaging (1 and 10 kpc) and spectroscopy (150 km s^{-1}) filters, normalized in three different ways: (1) to the total encounter time (see also Fig. B1); (2) to the time spent above the same filter (see also Figs B2 and B3); and (3) to the activity time spent above the same filter (see also Fig. 7). All numbers are fractions.

Run	1 kpc			10 kpc			150 km s^{-1}		
	(1)	(2)	(3)	(1)	(2)	(3)	(1)	(2)	(3)
01	0.126	0.137	0.262	0.062	0.086	0.192	0.024	0.083	0.187
02	0.037	0.044	0.125	0.023	0.037	0.127	0.010	0.045	0.141
03	0.089	0.097	0.265	0.017	0.024	0.091	0.009	0.038	0.116
04	0.051	0.080	0.269	0.005	0.011	0.050	0.007	0.032	0.105
05	0.072	0.096	0.313	0.006	0.010	0.050	0.017	0.077	0.227
06	0.080	0.087	0.184	0.052	0.071	0.155	0.040	0.152	0.268
07	0.027	0.029	0.110	0.003	0.004	0.022	0.010	0.051	0.169
08	0.012	0.023	0.087	0.006	0.014	0.081	0.003	0.020	0.074
09	0.007	0.008	0.052	0.001	0.001	0.018	0.002	0.015	0.068
10	0.004	0.005	0.019	0.002	0.003	0.017	0.001	0.007	0.024
C3	0.004	0.006	0.060	0.000	0.000	0.011	0.005	0.020	0.140
C4	0.085	0.097	0.201	0.042	0.062	0.156	0.032	0.134	0.275

together with all the other simulated encounters. The same numbers, together with other normalizations, are summarized in Table 2.

4.3.2 Initial geometry, gas fraction and black holes

The initial geometry, i.e. the angle between the galactic and global angular momentum vectors, is potentially important, because merger-induced tidal torques and ram-pressure shocks are most effective in coplanar encounters. To quantify these effects, we compare four 1:2 mergers: coplanar, prograde–prograde; retrograde–prograde; prograde–retrograde; and inclined–primary (Runs 02, 03, 04 and 05). We also separately compare two 1:4 mergers: coplanar, prograde–prograde and inclined–primary (Runs 07 and 08). Overall, the effect of geometry, once all other parameters are fixed, is not very significant, as the normalized dual-activity time-scales vary only by a factor of ~ 2 – 2.5 , with no clear trend: amongst the 1:2 mergers, the coplanar, prograde–prograde merger is the least active above 1 kpc and the most active above 10 kpc (see Fig. B5 for more details); the opposite happens for the 1:4 mergers (see Fig. B6).

The initial amount of gas is obviously very important, especially in isolated simulation like ours, where there is no replenishment from the cosmic web. The more gas is available, the more can potentially be funnelled towards the central BHs. In Runs 02 and 06, which differ only by the initial gas fraction in the disc (30 versus 60 per cent), overall, activity increases with gas availability, but not significantly: by a factor of ~ 1.2 – 1.9 , depending on the filter used (see Fig. B7 for more details).

BH parameters have obviously a direct effect on the dual-activity observability time-scales. Increasing the initial BH mass potentially increases luminosities, as BH accretion in our simulations scales as M_{BH}^2 [see equation (1)], but at the same time the additional power would increase AGN feedback, which is proportional to the luminosity. If we instead increase the BH feedback efficiency, i.e. the constant of proportionality with luminosity, the gas surrounding the BH is less cold and dense, causing BH accretion to decrease. To quantify these effects on the dual-activity observability time-scales, we compare Runs 02, C3 and C4, which differ only by the initial BH mass or feedback efficiency. Increasing the BH mass (by a factor of 2.5) increases the dual-activity time, but only by a factor $\lesssim 2$. Increasing the BH feedback efficiency (by a factor of 5) tends to decrease the normalized dual-activity time, although the factor widely depends on the filter one chooses (see Fig. B8 for more

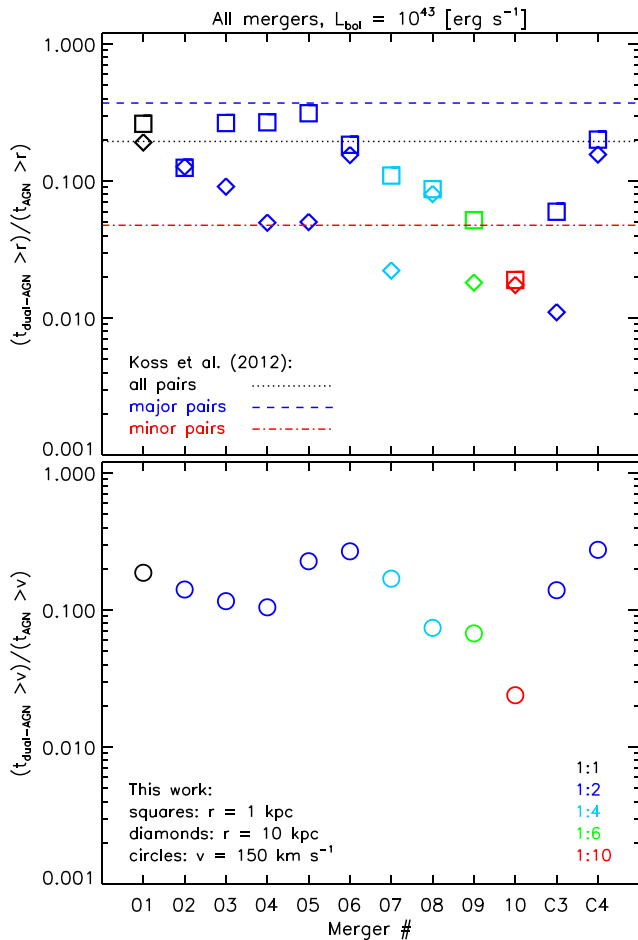


Figure 7. Dual-activity time above a given r (top panel: 1 kpc – squares – and 10 kpc – diamonds) and v (bottom panel: 150 km s^{−1} – circles), divided by the activity time above the same threshold, assuming a bolometric-luminosity threshold of 10⁴³ erg s^{−1}, for all the mergers in our suite. The merger number in the x -axis is the same as in Tables 1–2. The colours refer to the initial mass ratio: 1:1 – black, 1:2 – blue, 1:4 – cyan, 1:6 – green and 1:10 – red. The horizontal lines in the top panel show the observed fraction of dual AGN systems out of interacting systems (in which at least one system has an AGN) by Koss et al. (2012), for their full sample of BAT AGN (black, dot), their major pairs (blue, dash) and their minor pairs (red, dash-dot). Our major mergers with standard BH efficiency (squares of Runs 01–06 and C4) should be compared to the blue, dashed line, whereas our minor mergers (squares of Runs 07–10) should be compared to the red, dash-dotted line.

details). We note that different prescriptions for BH accretion (e.g. taking into account the angular momentum of the accreting gas; Debuhr et al. 2010; Hopkins & Quataert 2011; Anglés-Alcázar, Özel & Davé 2013; Anglés-Alcázar et al. 2015, 2017) or AGN feedback (e.g. Newton & Kay 2013; Wurster & Thacker 2013) may also affect the results.

4.4 Comparison with other work

In this section, we compare our dual-activity time-scales to a few select studies, both observational and theoretical, to validate our results.

4.4.1 Comparison with observations

Most surveys provide the total number of AGN pairs out of the total number of AGN (e.g. Shen et al. 2011). These results are difficult to compare to ours since, by construction, we do not simulate isolated galaxies that could be harbouring a single AGN.

Koss et al. (2012) study the fraction of dual AGN in the all-sky *Swift* Burst Alert Telescope (BAT) survey. For each of the 167 BAT AGN from the survey, they search for apparent companions, finding that 77 of them have at least a companion⁸ within 1–100 kpc. Of these 77 companions, 15 have an AGN, making the fraction of dual AGN systems out of interacting systems (in which at least one system has an AGN) equal to 19.5 per cent (15/77). If we divide their sample in major and minor pairs (defined as pairs with mass ratios $>$ and ≤ 0.25 , respectively), the fraction changes to 37.1 per cent (13/35) for the major pairs and to 4.8 per cent (2/42) for the minor pairs. Since in this case only interacting systems are considered, we can compare the numbers from Koss et al. (2012) to our results. To do that, we simply consider, for each of our mergers, the dual-activity time when the BHs are at $r > 1$ kpc (our galaxies, by construction, are never above $r \sim 90$ kpc) and divide it by the activity time at the same projected separations.⁹

In Fig. 7, we show the normalized dual-activity time above 1 kpc, 10 kpc and 150 km s^{−1}, for all our simulated mergers. We also show the results of Koss et al. (2012) for their full sample of BAT AGN and their subsamples of major and minor pairs. If we neglect the 1:2 merger with high BH feedback efficiency (Run C3), which obviously has a much lower accretion rate (see Section 4.3.2 and Capelo et al. 2015), our results are within a factor of ~ 2 from the result of Koss et al. (2012), for both major and minor mergers. We caution the reader that our definitions of activity are very different (we impose a simple luminosity threshold, whereas they use a variety of diagnostics). We also recover the trends found in Koss et al. (2012; see their fig. 2), when we split our results by distance or by mass ratio: the fraction of dual AGN increases with decreasing separation and increasing mass ratio (if we assume that galaxy and BH mass ratio are correlated also in observational samples).

Comerford et al. (2015), in their study of optically selected dual-AGN candidates, find that all their dual (and dual/offset) AGN systems have $f_{\text{Edd},1}/f_{\text{Edd},2} < 1$, that is the AGN in the less luminous stellar bulge (assuming that BH masses trace their host’s stellar bulge luminosity) has the higher specific accretion rate. This is equivalent to stating $dq/dt > 0$, where $q \equiv M_{\text{BH},2}/M_{\text{BH},1}$. We have already studied the dependence of q with time (Capelo et al. 2015) and found that, during the merger stage, which is when dual activity is more frequent, typically $dq/dt < 0$ for major mergers and > 0 for minor mergers, indicating that not all our dual AGN have $f_{\text{Edd},1}/f_{\text{Edd},2} < 1$. We note, however, that the only clear dual AGN in Comerford et al. (2015) is a minor merger.

⁸ For this and the following numbers, we refer to the online-only version of table 1 of Koss et al. (2012). When a BAT AGN has more than one companion, we consider only the pair with the largest M/r^2 , where M is the mass of the BAT AGN’s companion and r is the projected separation.

⁹ We do not consider the additional velocity-difference filter $v < 300$ km s^{−1} performed by Koss et al. (2012) – done to avoid contamination from the Hubble flow – because the time spent above 300 km s^{−1} is negligible (see Figs 3 and 4).

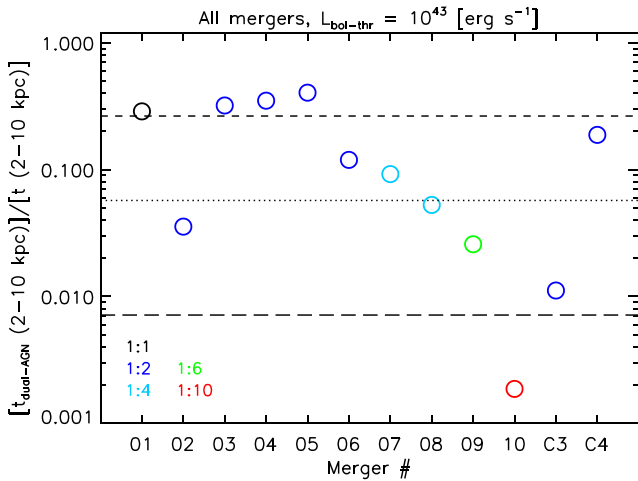


Figure 8. Same as the top panel of Fig. 7, but for the ratio of dual-activity time to merger time, in the projected-separation range 2–10 kpc. The horizontal, dashed line shows the result of Steinborn et al. (2016), whereas the horizontal, long-dashed and dotted lines show the results of Volonteri et al. (2016) for galaxies with galaxy masses greater than $10^{10} M_{\odot}$ at redshifts 0 and 2, respectively.

4.4.2 Comparison with simulations

We begin comparing our results to those of Van Wassenhove et al. (2012), since our setup is very similar to theirs. Taking the typical bolometric-luminosity threshold of $10^{43} \text{ erg s}^{-1}$, we obtain a dual-activity time equal to 16.8 per cent of the activity time, compared with their 16.3 per cent (we only compare the *total* numbers, i.e. when $r = v = 0$, since we use projected quantities and Van Wassenhove et al. 2012 use 3D quantities).

We then compare our results to recent cosmological studies that, although lacking in resolution and the ability to control parameters, have the advantage of modelling relatively large volumes and therefore increasing the number of galaxies one can study.

Steinborn et al. (2016) employ a cosmological simulation with a large volume of $(182 \text{ Mpc})^3$ from the set of the Magneticum Pathfinder Simulations, using the TreePM-SPH code GADGET3 (Springel 2005) and running it up to $z = 2$. If we assume that our encounters start at $z = 3$, then our major mergers (which last $\sim 1 \text{ Gyr}$) are thought to be at the same final redshift considered in Steinborn et al. (2016). From the simulation data, they count 34 BH pairs (defined as two BHs with a 3D separation in the range 2–10 kpc), of which 9 are dual AGN (with an AGN defined as a BH with bolometric luminosity higher than $10^{43} \text{ erg s}^{-1}$). Since the pairs are not chosen, as it was in the case of Koss et al. (2012), starting from one AGN and then looking for a companion, we need to compare their results to a different normalization: the dual-activity time divided by the merger time, for projected separations of 2–10 kpc.

The results are shown in Fig. 8. Each symbol represents one of the simulated encounters, whereas the horizontal, dashed line shows the result by Steinborn et al. (2016): 26.5 per cent dual-AGN fraction. The dual AGN in Steinborn et al. (2016) are mostly major (seven out of nine have a mass ratio greater than 0.25) and all our major mergers with standard BH feedback efficiency (except for one) are within a factor of ~ 2 from their result. We caution that the galaxy and BH masses considered in Steinborn et al. (2016) are higher than ours. Nevertheless, we are consistent with their result. For further comparison, we also show the results for galaxies with galaxy mass

$> 10^{10} M_{\odot}$ at redshifts 0 and 2 from the Horizon-AGN simulation (Volonteri et al. 2016). We caution the reader that, even though they use the same bolometric-luminosity threshold ($10^{43} \text{ erg s}^{-1}$) as in Steinborn et al. (2016), they do not use a fixed separation threshold.

We also checked the trends found in Steinborn et al. (2016; see their fig. 3), when we split our results by (cumulative) distance: they find a flat distribution of dual-AGN fraction for separations between 5 and 10 kpc and an increase for lower separations. Overall, we also not only find an increase with decreasing separation but also see a somewhat flatter distribution.

5 CONCLUSIONS

We performed a large suite of high-resolution hydrodynamical simulations of galaxy mergers, where we vary the initial mass ratio, geometry, gas fraction and BH parameters, to investigate the triggering of dual AGN. Using different thresholds (bolometric and hard-X-ray luminosity and Eddington ratio) and, in the case of X-rays, accounting for obscuration from gas and contamination from star formation, we computed the dual-activity observability time-scales for each of our 12 mergers, as a function of projected BH separation and velocity difference. We also assessed the importance of each phase in the history of the mergers and applied thresholds (to both projected separations and velocity differences) to mimic observational-resolution limitations. Finally, we studied the effects of changing merger, galactic and BH parameters and compared our results to both observational and theoretical works.

We itemize our findings below.

(i) Dual BH activity is generally low during the stochastic and remnant stages and increases during the merger stage, especially at or right after late pericentric passages (Fig. 1 and Table B1). At low luminosity thresholds, dual activity follows the history of the entire encounter. At high thresholds, it roughly follows the history of the merger phase. During the remnant stage, the separations and velocity differences between the two BHs are too small for detection (Figs 2–4).

(ii) When accounting for gas obscuration in the case of hard-X-ray (2–10 keV) observations, we find that the decrease in dual-activity time is negligible when we assume the galaxies to be at high redshift ($z \sim 3$) and moderate (a factor of ~ 2) if our simulated galaxies are representative of relatively small, gas-rich local galaxies (Fig. 5). Contamination from star formation is always irrelevant.

(iii) Using projected BH separations (r) and velocity differences (v) rather than 3D quantities produces very different results, especially when one filters by velocity difference (mimicking spectroscopic observations): the decrease in dual-activity time can be as high as a factor of ~ 4 (Figs A2–A3).

(iv) The normalized dual-activity time – defined as the dual-activity time divided by the activity time spent above the same r or v filter – for the default merger (of a mass ratio 1:2) is 12.5–14.1 per cent, depending on the filter.

(v) The normalized dual-activity time increases with increasing mass ratio (with the factor increasing with the threshold, ranging from factors of a few to orders of magnitude), is independent of r at low luminosities and is non-negligible only at small r at high luminosities: in order to identify dual AGN, shallow surveys will be more affected by an increase of angular resolution, with respect to deeper surveys (Fig. 6 and Table 2).

(vi) The normalized dual-activity time does not heavily depend on the geometry of the encounters, with the difference between mergers being only a factor of ~ 2 – 2.5 and with no clear trend. Doubling the initial amount of gas increases the time, but only by a factor of ~ 1.2 – 1.9 , depending on the filter used. Roughly doubling the initial BH mass increases the time by a factor of $\lesssim 2$, whereas quintupling the BH feedback efficiency parameter decreases it, although the factor depends widely on the filter used (Figs 7 and B5–B8, and Table 2).

(vii) The results from our idealized merger simulations are consistent with observations, with the normalized dual-activity time of our mergers with standard BH feedback efficiency being within a factor of ~ 2 from that of comparable systems observed in Koss et al. (2012; Fig. 7), for both major and minor encounters. They are also consistent with cosmological simulations, with all our major mergers with standard BH feedback efficiency (except for one) within a factor of ~ 2 from those simulated in Steinborn et al. (2016; Fig. 8).

We caution that all our estimates are upper limits, as we have not included the effects of dust obscuration from the torus/broad line region in the vicinity of the BH, which cannot be resolved in our suite of simulations. Moreover, given our temporal (0.1 Myr) and spatial (~ 10 pc) resolution, we cannot account for variability on smaller time-scales and spatial scales than those, possibly overestimating the dual-AGN time, as more accretion becomes non-simultaneous (Hopkins & Quataert 2010; Levine, Gnedin & Hamilton 2010). Future numerical studies with improved resolution should partially alleviate these issues. We also note that our results may be sensitive to different treatments of BH accretion (e.g. Debuhr et al. 2010; Hopkins & Quataert 2011; Anglés-Alcázar et al. 2013, 2015, 2017), AGN feedback (e.g. Newton & Kay 2013; Wurster & Thacker 2013), or the numerical method employed (e.g. Hayward et al. 2014). A thorough analysis of the dependence of the results on all these aspects is not within the scope of the current work and will be addressed in a future work.

Another aspect that warrants future investigation is the dependence of our results on galaxy mass. More massive merging galaxies may be able to form circumnuclear discs (CNDs), as suggested by both observations (Downes & Solomon 1998; Medling et al. 2014) and simulations (Mayer, Kazantzidis & Escala 2008; Roškar et al. 2015). The presence of the CND would affect the gas flow around the BHs, hence their accretion history, and could also play a role in obscuration originating at scales larger than the scale of the tori (Hopkins et al. 2012). These effects would have an impact on the dual-AGN time-scales. Yet, based on the results of pc-scale merger simulations (Roškar et al. 2015), we argue that CNDs would probably form at the end of the remnant phase studied in this work. Therefore, our results, which concern the previous evolutionary phase of the massive BH pair, should not be affected.

Another avenue of research is to study the activity of BH pairs in massive (stellar mass greater than $10^{10} M_{\odot}$) galaxies at $z > 1$, which, being more dense and clumpy, might be a favourable environment for dual-AGN activity. In such galaxies, the orbital decay of massive BH pairs has been shown to be inefficient at separations of a few hundred pc to a kpc, due to the perturbations of the clumpy interstellar medium on to the BH pair (Tamburello et al. 2017). The latter effect could lengthen the duration of the dual-activity phase after the galaxy merger has been completed. We note, however, that the galaxy mass range we investigate here is statistically more relevant across cosmic epochs, since more massive galaxies are rare at $z > 1$. Moreover, at low redshift, disc galaxies exhibit relatively smooth discs even at the largest mass scales.

ACKNOWLEDGEMENTS

We thank the reviewer for the useful comments that greatly improved this work. We also thank Andrea Comastri, Davide Fiacconi, Carmen Montuori, Thomas R. Quinn and Sandor Van Wassenhove for their help and useful discussions. MV acknowledges funding support from NASA, through award ATP NNX10AC84G, from SAO, through award TM1-12007X, from NSF, through award AST 1107675, and from the European Research Council under the European Community's Seventh Framework Programme (FP7/2007-2013 Grant Agreement no. 614199, project 'BLACK'). Resources supporting this work were provided by the NASA High-End Computing (HEC) Program through the NASA Advanced Supercomputing (NAS) Division at Ames Research Center, and by TGCC, under the allocations 2013-t2013046955 and 2014-x2014046955 made by GENCI. This research was supported in part by the National Science Foundation under grant no. NSF PHY11-25915, through the Kavli Institute for Theoretical Physics and its program 'A Universe of Black Holes'. PRC thanks the Institut d'Astrophysique de Paris for hosting him during his visits and acknowledges support by the Tomalla foundation.

REFERENCES

- Anglés-Alcázar D., Özel F., Davé R., 2013, *ApJ*, 770, 5
- Anglés-Alcázar D., Özel F., Davé R., Katz N., Kollmeier J. A., Oppenheimer B. D., 2015, *ApJ*, 800, 127
- Anglés-Alcázar D., Davé R., Faucher-Giguère C.-A., Özel F., Hopkins P. F., 2017, *MNRAS*, 464, 2840
- Bellovary J. M., Governato F., Quinn T. R., Wadsley J., Shen S., Volonteri M., 2010, *ApJ*, 721, L148
- Benson A. J., 2005, *MNRAS*, 358, 551
- Blecha L., Loeb A., Narayan R., 2013, *MNRAS*, 429, 2594
- Blumenthal G. R., Faber S. M., Primack J. R., Rees M. J., 1984, *Nature*, 311, 517
- Bondi H., 1952, *MNRAS*, 112, 195
- Bondi H., Hoyle F., 1944, *MNRAS*, 104, 273
- Callegari S., Mayer L., Kazantzidis S., Colpi M., Governato F., Quinn T., Wadsley J., 2009, *ApJ*, 696, L89
- Callegari S., Kazantzidis S., Mayer L., Colpi M., Bellovary J. M., Quinn T., Wadsley J., 2011, *ApJ*, 729, 85
- Camm G. L., 1950, *MNRAS*, 110, 305
- Capelo P. R., Dotti M., 2017, *MNRAS*, 465, 2643
- Capelo P. R., Volonteri M., Dotti M., Bellovary J. M., Mayer L., Governato F., 2015, *MNRAS*, 447, 2123
- Comerford J. M., Pooley D., Barrows R. S., Greene J. E., Zakamska N. L., Madejski G. M., Cooper M. C., 2015, *ApJ*, 806, 219
- Debuhr J., Quataert E., Ma C.-P., Hopkins P., 2010, *MNRAS*, 406, L55
- Di Matteo T., Springel V., Hernquist L., 2005, *Nature*, 433, 604
- Downes D., Solomon P. M., 1998, *ApJ*, 507, 615
- Ellison S. L., Patton D. R., Mendel J. T., Scudder J. M., 2011, *MNRAS*, 418, 2043
- Ellison S. L., Mendel J. T., Patton D. R., Scudder J. M., 2013, *MNRAS*, 435, 3627
- Ferrarese L., Ford H., 2005, *Space Science Reviews*, 116, 523
- Fu H. et al., 2011, *ApJ*, 740, L44
- Gabányi K. É., An T., Frey S., Komossa S., Paragi Z., Hong X.-Y., Shen Z.-Q., 2016, *ApJ*, 826, 106
- Gabor J. M., Capelo P. R., Volonteri M., Bournaud F., Bellovary J., Governato F., Quinn T., 2016, *A&A*, 592, A62
- Grimm H.-J., Gilfanov M., Sunyaev R., 2003, *MNRAS*, 339, 793
- Hayward C. C., Torrey P., Springel V., Hernquist L., Vogelsberger M., 2014, *MNRAS*, 442, 1992
- Hennawi J. F. et al., 2010, *ApJ*, 719, 1672
- Hernquist L., 1990, *ApJ*, 356, 359
- Hopkins P. F., Quataert E., 2010, *MNRAS*, 407, 1529

- Hopkins P. F., Quataert E., 2011, *MNRAS*, 415, 1027
- Hopkins P. F., Hernquist L., Cox T. J., Di Matteo T., Robertson B., Springel V., 2006, *ApJS*, 163, 1
- Hopkins P. F., Richards G. T., Hernquist L., 2007, *ApJ*, 654, 731
- Hopkins P. F., Hayward C. C., Narayanan D., Hernquist L., 2012, *MNRAS*, 420, 320
- Hoyle F., Lyttleton R. A., 1939, *Proceedings of the Cambridge Philosophical Society*, 35, 405
- Johansson P. H., Burkert A., Naab T., 2009, *ApJ*, 707, L184
- Khochfar S., Burkert A., 2006, *A&A*, 445, 403
- Komossa S., Zensus J. A., 2016, in Meiron Y., Li S., Liu F.-K., Spurzem R., eds, *Proc. IAU Symp. Vol. 312, Star Clusters and Black Holes in Galaxies across Cosmic Time*. Cambridge Univ. Press, Cambridge, pp 13
- Kormendy J., Richstone D., 1995, *ARA&A*, 33, 581
- Koss M., Mushotzky R., Treister E., Veilleux S., Vasudevan R., Trippe M., 2012, *ApJ*, 746, L22
- Koss M. J. et al., 2016, *ApJ*, 824, L4
- Levine R., Gnedin N. Y., Hamilton A. J. S., 2010, *ApJ*, 716, 1386
- Liu X., Shen Y., Strauss M. A., Hao L., 2011, *ApJ*, 737, 101
- Liu X., Civano F., Shen Y., Green P., Greene J. E., Strauss M. A., 2013, *ApJ*, 762, 110
- Marconi A., Hunt L. K., 2003, *ApJ*, 589, L21
- Mayer L., Kazantzidis S., Escala A., 2008, *Mem. Soc. Astron. Italiana*, 79, 1284
- Medling A. M. et al., 2014, *ApJ*, 784, 70
- Merloni A. et al., 2010, *ApJ*, 708, 137
- Mukai K., 1993, *Legacy*, 3, 21–31, 3, 21
- Müller-Sánchez F., Comerford J. M., Nevin R., Barrows R. S., Cooper M. C., Greene J. E., 2015, *ApJ*, 813, 103
- Myers A. D., Richards G. T., Brunner R. J., Schneider D. P., Strand N. E., Hall P. B., Blomquist J. A., York D. G., 2008, *ApJ*, 678, 635
- Navarro J. F., Frenk C. S., White S. D. M., 1996, *ApJ*, 462, 563
- Newton R. D. A., Kay S. T., 2013, *MNRAS*, 434, 3606
- Pfister H., Lupi A., Capelo P. R., Volonteri M., Bellovary J. M., Dotti M., 2017, preprint ([arXiv:1706.04010](https://arxiv.org/abs/1706.04010))
- Roškar R., Fiacconi D., Mayer L., Kazantzidis S., Quinn T. R., Wadsley J., 2015, *MNRAS*, 449, 494
- Shakura N. I., Sunyaev R. A., 1973, *A&A*, 24, 337
- Shen S., Wadsley J., Stinson G., 2010, *MNRAS*, 407, 1581
- Shen Y., Liu X., Greene J. E., Strauss M. A., 2011, *ApJ*, 735, 48
- Silverman J. D. et al., 2011, *ApJ*, 743, 2
- Spitzer L., Jr, 1942, *ApJ*, 95, 329
- Springel V., 2005, *MNRAS*, 364, 1105
- Springel V., Hernquist L., 2003, *MNRAS*, 339, 289
- Springel V., White S. D. M., 1999, *MNRAS*, 307, 162
- Stadel J. G., 2001, PhD thesis, Univ. Washington
- Steinborn L. K., Dolag K., Comerford J. M., Hirschmann M., Remus R.-S., Teklu A. F., 2016, *MNRAS*, 458, 1013
- Stinson G., Seth A., Katz N., Wadsley J., Governato F., Quinn T., 2006, *MNRAS*, 373, 1074
- Tamburello V., Capelo P. R., Mayer L., Bellovary J. M., Wadsley J. W., 2017, *MNRAS*, 464, 2952
- Tingay S. J., Wayth R. B., 2011, *AJ*, 141, 174
- Tremmel M., Governato F., Volonteri M., Quinn T. R., 2015, *MNRAS*, 451, 1868
- Tremmel M., Karcher M., Governato F., Volonteri M., Quinn T., Pontzen A., Anderson L., 2016, *MNRAS*, preprint ([arXiv:1607.02151](https://arxiv.org/abs/1607.02151))
- Van Wassenhove S., Volonteri M., Mayer L., Dotti M., Bellovary J., Callegari S., 2012, *ApJ*, 748, L7
- Van Wassenhove S., Capelo P. R., Volonteri M., Dotti M., Bellovary J. M., Mayer L., Governato F., 2014, *MNRAS*, 439, 474
- Volonteri M., Capelo P. R., Netzer H., Bellovary J., Dotti M., Governato F., 2015a, *MNRAS*, 449, 1470
- Volonteri M., Capelo P. R., Netzer H., Bellovary J., Dotti M., Governato F., 2015b, *MNRAS*, 452, L6
- Volonteri M., Dubois Y., Pichon C., Devriendt J., 2016, *MNRAS*, 460, 2979
- Wadsley J. W., Stadel J., Quinn T., 2004, *New Astron.*, 9, 137
- Wurster J., Thacker R. J., 2013, *MNRAS*, 431, 2513
- Younger J. D., Hopkins P. F., Cox T. J., Hernquist L., 2008, *ApJ*, 686, 815

SUPPORTING INFORMATION

Supplementary data are available at [MNRAS](https://www.mnras.org) online.

dualagnpaper_20170421_mnras_supp.pdf

Please note: Oxford University Press is not responsible for the content or functionality of any supporting materials supplied by the authors. Any queries (other than missing material) should be directed to the corresponding author for the article.

APPENDIX A: EFFECTS OF PROJECTION AND RESOLUTION

In this section, we show the effects of using projected lines of sight as opposed to 3D quantities.

In Fig. A1, we show the normalized distributions of the magnitude of projected vectors, for the two cases when we project a vector on to a random line of sight (in this work: velocity difference) and when we project a vector on to the plane perpendicular to a random line of sight (in this work: separation). In the former case, the probability distribution is flat. In the latter, the probability distribution is skewed towards large values, i.e. the magnitude of the 3D vector. As an example, the probability that the magnitude of the projected vector is less than 80 per cent of that of the 3D vector is 80 per cent in the v case and 40 per cent in the r case.

In Fig. A2, we quantify the effects of projection, by showing the dual-activity observability time-scales in the default merger using 3D quantities and projected quantities, based on 10, 100 and 1000 random lines of sight. The results with 100 and 1000 lines of sight are indistinguishable, which justifies our use of 100 lines of sight throughout the analysis. On the other hand, using a lower number of random lines of sight (e.g. 10) or even 3D quantities can give results that are different by up to a factor of 3–4 in the v -plots and are similar in the r -plots (except for very high luminosity thresholds).

In Fig. A3, we show the dual-activity observability time-scales as a function of r and v , and of r and $L_{\text{bol},1}/L_{\text{bol},2}$, in the same way as shown in Fig. 4, this time using 3D quantities (as used in Van Wassenhove et al. 2012). The difference in the ‘ v versus r ’ plots is striking. For example, from looking at the $L_{\text{bol}} = 10^{42.5}$ results of Fig. A3, one would expect to find a relatively large population of systems at large separations ($\gtrsim 40$ kpc; before the first pericentric passage) with high-velocity differences (around 180–300 km s^{-1}), an ideal case for current spectroscopic surveys.

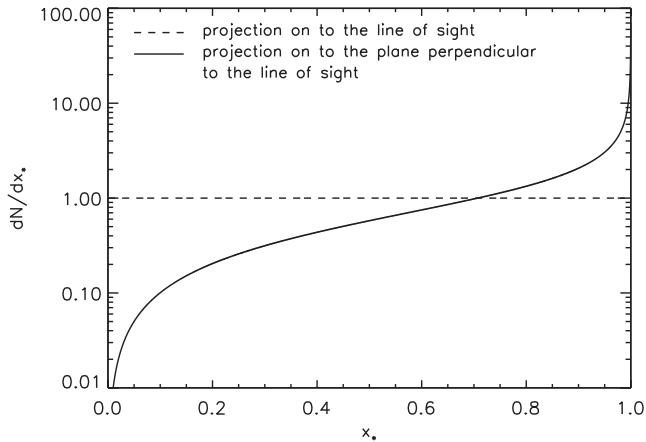


Figure A1. Normalized probability distributions of the magnitude $x_* \equiv x/x_{3D}$ of projected vectors, for two different projections of a given 3D vector of magnitude x_{3D} . (a) Projection on to the line of sight (in this work: velocity difference; dashed line): $dN/dx = 1/x_{3D}$; (b) Projection on to the plane perpendicular to the line of sight (in this work: separation; solid line): $dN/dx = (x/x_{3D}^2)/\sqrt{1 - (x/x_{3D})^2}$.

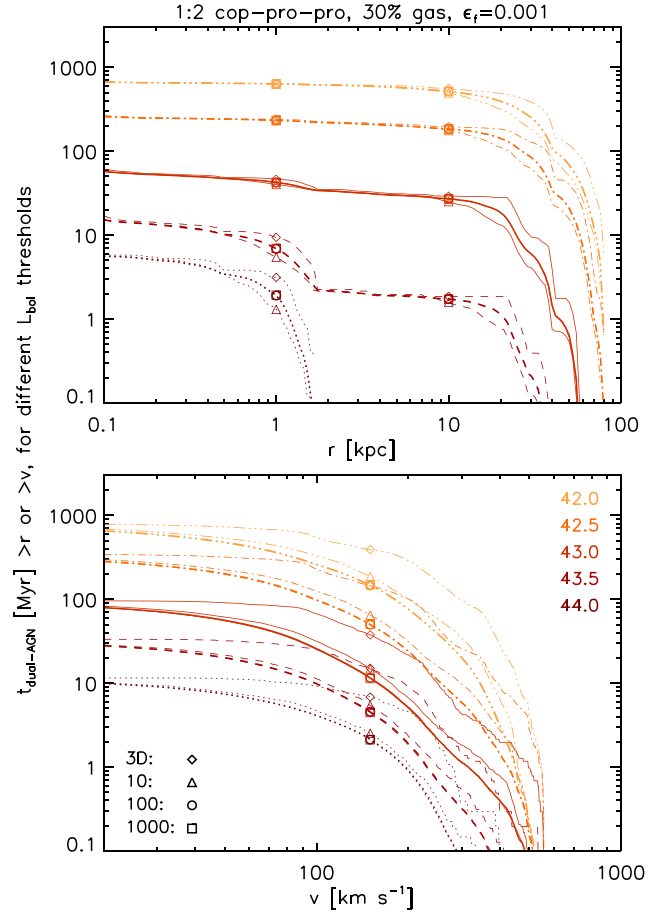


Figure A2. Same as the left panels of Fig. 3, but using 3D quantities and different numbers of lines of sight. The symbols refer to the following projected separations and velocity differences: 1 and 10 kpc and 150 km s^{-1} . For each luminosity threshold, we show four lines: 1000 (thin lines and squares), 100 (thick lines and circles), and 10 lines of sight (thin lines and triangles), and 3D quantities (thin lines and diamonds). As expected, the 3D time is always higher than the projected times, although the projection does not change significantly the r -plots. On the other hand, the time-decrease factor in the v -plots can be as much as 3–4. The difference between using 100 and 1000 lines of sight is negligible.

However, if we consider the effects of projection (see Fig. 4), the result changes dramatically, with the dual-activity time in the same region of velocity–separation phase-space basically going to zero.

We note that our results change when we degrade the resolution, as already shown in Volonteri et al. (2015a). At low resolution, we cannot resolve small-scale gravitational torques and overdensities. This leads, in the case of the default merger, to a BH accretion rate generally higher than that of the high-resolution run, where the region near the BHs is better resolved, causing an increase in the dual-activity time-scales. For more details on the effects of resolution, we refer the reader to the appendix of Volonteri et al. (2015a).

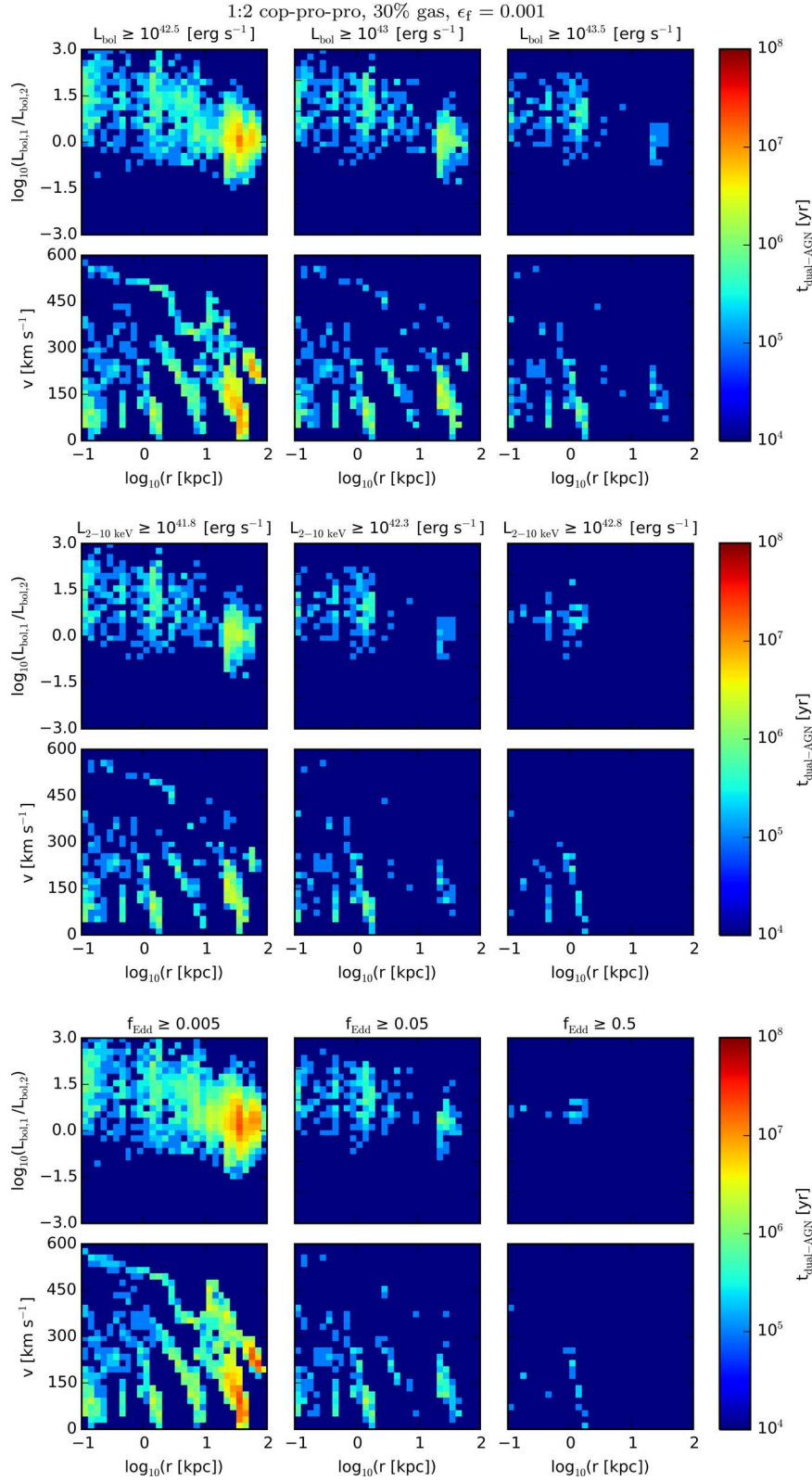


Figure A3. Same as Fig. 4, using 3D quantities.

APPENDIX B: ADDITIONAL FIGURES AND TABLE

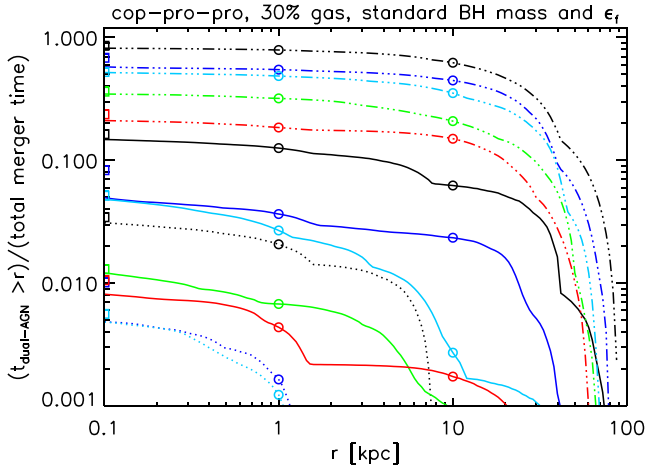


Figure B1. Same as Fig. 6, except that we divide the dual-activity time above a given BH projected separation by the total merger time. At $r = 1$ kpc, the normalized dual-activity time is highest for the 1:1 merger, followed by the 1:2, 1:4, 1:6 and 1:10 mergers, regardless of the luminosity threshold shown.

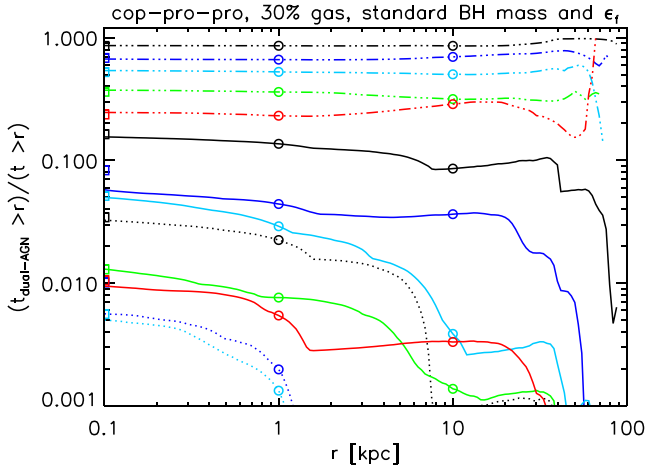


Figure B2. Same as Fig. 6, except that we divide the dual-activity time above a given BH projected separation by the time spent above the same r . At $r = 1$ kpc, the normalized dual-activity time is highest for the 1:1 merger, followed by the 1:2, 1:4, 1:6 and 1:10 mergers, regardless of the luminosity threshold shown.

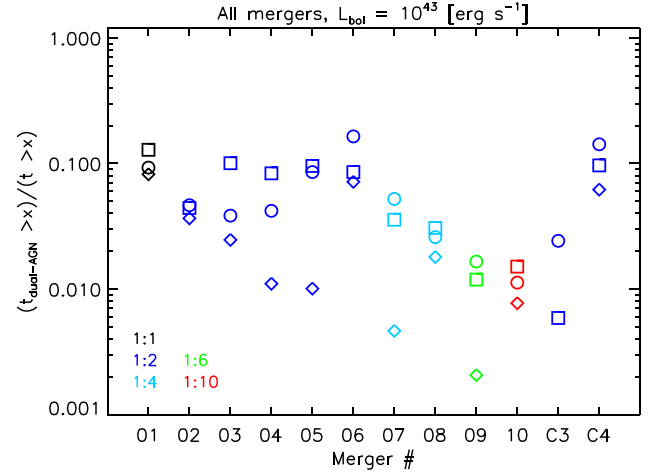


Figure B3. Same as Fig. 7, except that we divide the dual-activity time above a given r and v by the time above the same threshold (and use one panel).

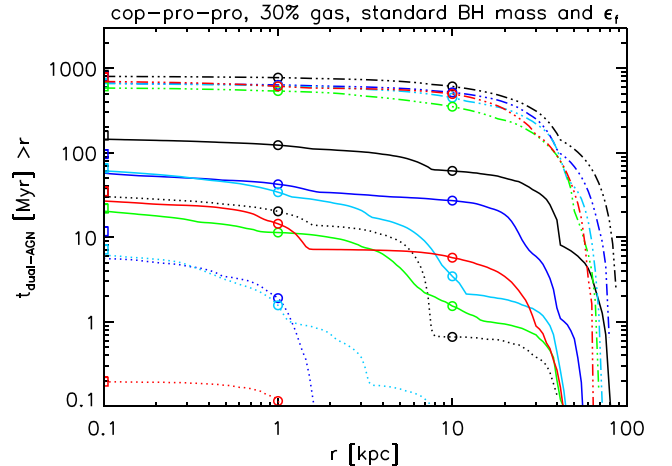


Figure B4. Same as Fig. 6, except that we do not normalize the time. At $r = 1$ kpc, the dual-activity time is highest for the 1:1 merger, followed by the 1:2, 1:4, 1:10 and 1:6 mergers, regardless of the luminosity threshold shown.

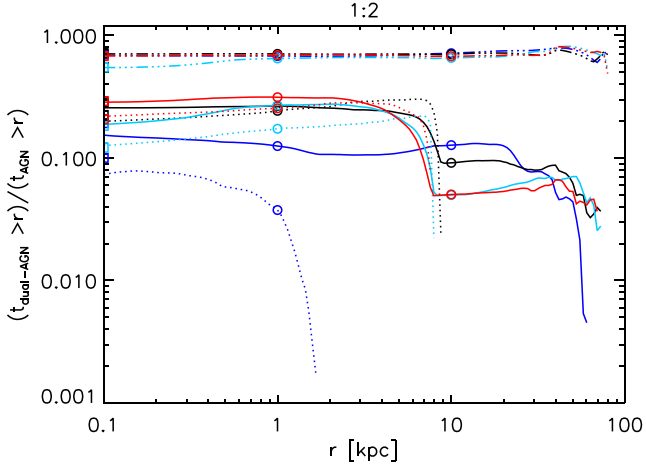


Figure B5. Same as Fig. 6, but for the 1:2 coplanar, prograde-prograde mergers with 30 per cent gas fraction, standard BH mass and feedback efficiency, and different geometries (coplanar, prograde-prograde: blue, total encounter time 1.158 Gyr; inclined-primary: black, 1.085 Gyr; coplanar, retrograde-prograde: cyan, 1.579 Gyr; and coplanar, prograde-retrograde: red, 1.266 Gyr). At $r = 1$ kpc, the normalized dual-activity time for $L_{\text{thr}} = 10^{42} \text{ erg s}^{-1}$ is highest for the inclined-primary merger, followed by the prograde-retrograde, prograde-prograde, and retrograde-prograde mergers. For $L_{\text{thr}} = 10^{43} \text{ erg s}^{-1}$, it is highest for the prograde-retrograde merger, followed by the retrograde-prograde, inclined-primary and prograde-prograde mergers. For $L_{\text{thr}} = 10^{44} \text{ erg s}^{-1}$, it is highest for the prograde-retrograde merger, followed by the inclined-primary, retrograde-prograde and prograde-prograde mergers.

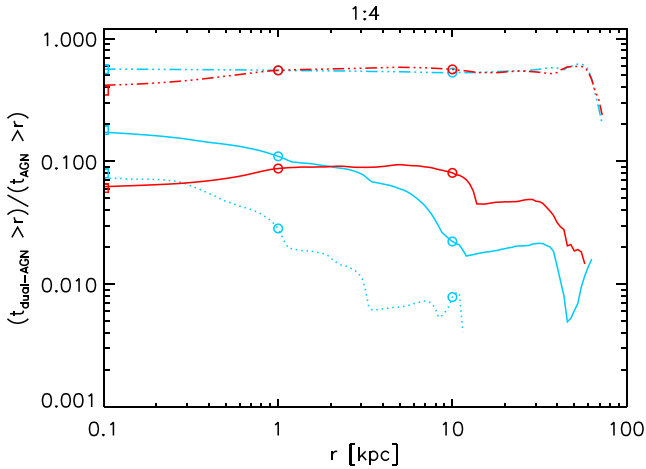


Figure B6. Same as Fig. 6, but for the 1:4 coplanar, prograde-prograde mergers with 30 per cent gas fraction, standard BH mass and feedback efficiency, and different geometries (coplanar, prograde-prograde: cyan, total encounter time 1.271 Gyr; and inclined-primary: red, 2.357 Gyr). At $r = 0.1$ kpc, the normalized dual-activity time is highest for the coplanar merger, regardless of the luminosity threshold shown.

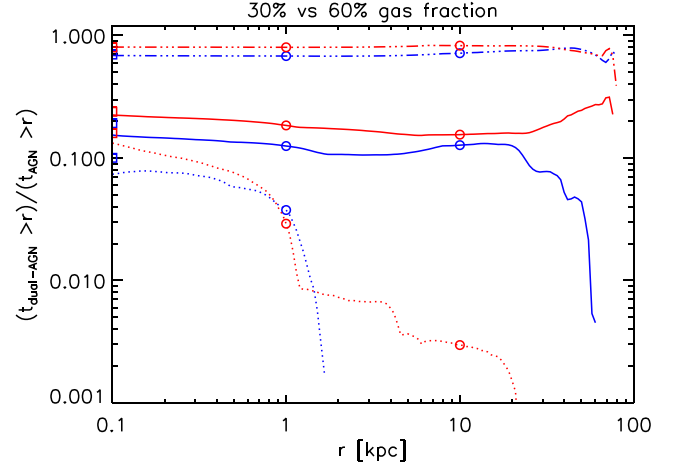


Figure B7. Same as Fig. 6, but for the 1:2 coplanar, prograde-prograde merger with 30 (blue; total encounter time 1.158 Gyr) and 60 (red; 1.022 Gyr) per cent gas fraction, and standard BH mass and feedback efficiency. At $r = 10$ kpc, the normalized dual-activity time is highest for the 60-per-cent gas-fraction merger, regardless of the luminosity threshold shown.

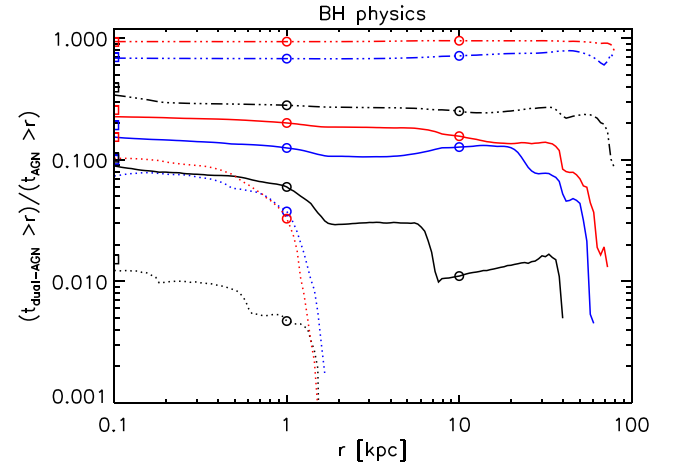


Figure B8. Same as Fig. 6, but for the 1:2 coplanar, prograde-prograde mergers with 30 per cent gas fraction and different BH parameters (standard BH mass and feedback efficiency: blue, total encounter time 1.158 Gyr; standard BH mass and high BH feedback efficiency: black, 1.281 Gyr; and large BH mass and standard BH feedback efficiency: red, 1.090 Gyr). At $r = 0.1$ kpc, the normalized dual-activity time is highest for the merger with large BH mass and standard BH feedback efficiency, followed by the merger with standard BH mass and feedback efficiency and by that with standard BH mass and high BH feedback efficiency, regardless of the luminosity threshold shown.

Table B1. Results for the 1:2 coplanar, prograde–prograde merger with 30 per cent gas fraction and standard BH mass and feedback efficiency (the default merger). The thresholds 41.3, 41.8, 42.3, 42.8 and 43.3 refer to $\log_{10}(L_{2-10\text{keV}} [\text{erg s}^{-1}])$; 0.005, 0.05 and 0.5 refer to f_{Edd} ; and 42.0, 42.5, 43.0, 43.5 and 44.0 refer to $\log_{10}(L_{\text{bol}} [\text{erg s}^{-1}])$. All times are given in Gyr and are either total (bottom section) or on a per-stage basis (top three sections). The number in parenthesis in the first column of each section is the duration of the stage (or of the total merger). Similar tables, for all other mergers, can be found in the online-only material.

Run 02	Threshold $L_{\text{thr}}/f_{\text{Edd}}$	BH ₁ above thr.	BH ₂ above thr.	Either BH above thr.	any d or v	Both BHs above the threshold		
						$d > 1 \text{ kpc}$	$d > 10 \text{ kpc}$	$v > 150 \text{ km s}^{-1}$
Stochastic (0.849)	41.30	0.591	0.442	0.719	0.315	0.312	0.278	0.060
	41.80	0.216	0.128	0.300	0.043	0.043	0.038	0.006
	42.30	0.039	0.021	0.058	0.002	0.002	0.002	0.000
	42.80	0.003	0.002	0.005	0.000	0.000	0.000	0.000
	43.30	0.000	0.000	0.000	0.000	0.000	0.000	0.000
	0.005	0.564	0.598	0.761	0.401	0.399	0.357	0.084
	0.050	0.055	0.070	0.118	0.007	0.007	0.006	0.001
	0.500	0.001	0.002	0.002	0.000	0.000	0.000	0.000
	42.00	0.763	0.651	0.827	0.587	0.584	0.518	0.129
	42.50	0.490	0.343	0.625	0.209	0.206	0.184	0.038
	43.00	0.177	0.101	0.248	0.031	0.031	0.027	0.004
	43.50	0.042	0.021	0.061	0.002	0.002	0.002	0.000
	44.00	0.006	0.003	0.009	0.000	0.000	0.000	0.000
Merger (0.206)	41.30	0.199	0.103	0.200	0.102	0.033	0.000	0.014
	41.80	0.182	0.063	0.184	0.061	0.014	0.000	0.008
	42.30	0.145	0.032	0.147	0.030	0.005	0.000	0.004
	42.80	0.092	0.010	0.094	0.008	0.001	0.000	0.002
	43.30	0.048	0.001	0.049	0.000	0.000	0.000	0.000
	0.005	0.189	0.113	0.196	0.106	0.038	0.000	0.015
	0.050	0.131	0.044	0.138	0.038	0.008	0.000	0.005
	0.500	0.038	0.007	0.042	0.003	0.001	0.000	0.001
	42.00	0.204	0.129	0.204	0.129	0.050	0.000	0.017
	42.50	0.196	0.093	0.197	0.092	0.027	0.000	0.012
	43.00	0.178	0.059	0.180	0.056	0.012	0.000	0.007
	43.50	0.146	0.033	0.148	0.031	0.005	0.000	0.004
	44.00	0.104	0.014	0.106	0.012	0.002	0.000	0.002
Remnant (0.103)	41.30	0.097	0.062	0.101	0.057	0.000	0.000	0.000
	41.80	0.062	0.028	0.079	0.012	0.000	0.000	0.000
	42.30	0.013	0.007	0.020	0.000	0.000	0.000	0.000
	42.80	0.001	0.001	0.001	0.000	0.000	0.000	0.000
	43.30	0.000	0.000	0.000	0.000	0.000	0.000	0.000
	0.005	0.045	0.062	0.086	0.021	0.000	0.000	0.000
	0.050	0.001	0.011	0.011	0.000	0.000	0.000	0.000
	0.500	0.000	0.000	0.000	0.000	0.000	0.000	0.000
	42.00	0.101	0.077	0.102	0.076	0.000	0.000	0.000
	42.50	0.090	0.053	0.099	0.045	0.000	0.000	0.000
	43.00	0.057	0.025	0.073	0.009	0.000	0.000	0.000
	43.50	0.014	0.007	0.020	0.000	0.000	0.000	0.000
	44.00	0.001	0.001	0.002	0.000	0.000	0.000	0.000
Total (1.158)	41.30	0.887	0.607	1.020	0.474	0.345	0.278	0.074
	41.80	0.460	0.219	0.563	0.116	0.056	0.038	0.014
	42.30	0.197	0.059	0.224	0.033	0.007	0.002	0.005
	42.80	0.096	0.013	0.100	0.008	0.001	0.000	0.002
	43.30	0.048	0.001	0.049	0.000	0.000	0.000	0.000
	0.005	0.798	0.773	1.043	0.529	0.437	0.357	0.099
	0.050	0.187	0.125	0.267	0.045	0.015	0.006	0.006
	0.500	0.039	0.008	0.045	0.003	0.001	0.000	0.001
	42.00	1.068	0.857	1.134	0.792	0.634	0.518	0.147
	42.50	0.777	0.490	0.921	0.345	0.234	0.184	0.050
	43.00	0.412	0.185	0.501	0.096	0.042	0.027	0.012
	43.50	0.201	0.061	0.229	0.034	0.007	0.002	0.005
	44.00	0.111	0.018	0.117	0.012	0.002	0.000	0.002

This paper has been typeset from a \LaTeX file prepared by the author.